



PAPER • OPEN ACCESS

## Coexistence of asynchronous and clustered dynamics in noisy inhibitory neural networks

To cite this article: Yannick Feld *et al* 2024 *New J. Phys.* **26** 063017

View the [article online](#) for updates and enhancements.

You may also like

- [LOCC convertibility of entangled states in infinite-dimensional systems](#)  
César Massri, Guido Bellomo, Hector Freytes et al.
- [Influence of different annealing ambient on terbium oxide passivation layers sputtered using the RF sputtering on silicon substrate](#)  
Abubakar Sifawa Abdullahi, Sabah M. Mohammad, Aminu Muhammad et al.
- [Characterization of OH species in kHz air/H<sub>2</sub>O atmospheric pressure dielectric barrier discharges](#)  
Cheng-Liang Huang, Tzu-Yi Liao, Yi-Ting He et al.



## PAPER




# Coexistence of asynchronous and clustered dynamics in noisy inhibitory neural networks

## OPEN ACCESS

RECEIVED  
9 February 2024REVISED  
11 May 2024ACCEPTED FOR PUBLICATION  
20 May 2024PUBLISHED  
12 June 2024

Original Content from  
this work may be used  
under the terms of the  
[Creative Commons  
Attribution 4.0 licence](#).

Any further distribution  
of this work must  
maintain attribution to  
the author(s) and the title  
of the work, journal  
citation and DOI.

Yannick Feld<sup>1,2</sup> , Alexander K Hartmann<sup>2</sup>  and Alessandro Torcini<sup>3,4,\*</sup> <sup>1</sup> Université Paris-Saclay, CNRS, CEA, Institut de Physique Théorique, 91191 Gif-sur-Yvette, France<sup>2</sup> Institut für Physik, Carl von Ossietzky Universität Oldenburg, 26111 Oldenburg, Germany<sup>3</sup> Laboratoire de Physique Théorique et Modélisation, CY Cergy Paris Université, CNRS, UMR 8089, 95302 Cergy-Pontoise cedex, France<sup>4</sup> CNR—Consiglio Nazionale delle Ricerche—Istituto dei Sistemi Complessi, via Madonna del Piano 10, 50019 Sesto Fiorentino, Italy

\* Author to whom any correspondence should be addressed.

E-mail: [alessandro.torcini@isc.cnr.it](mailto:alessandro.torcini@isc.cnr.it), [yannick.feld@ipht.fr](mailto:yannick.feld@ipht.fr) and [a.hartmann@uni-oldenburg.de](mailto:a.hartmann@uni-oldenburg.de)**Keywords:** spiking neural networks, inhibition, noise, neural mass model, quadratic integrate-and-fire neuron, cluster synchronisation,  $\gamma$ -oscillations

## Abstract

A regime of coexistence of asynchronous and clustered dynamics is analysed for globally coupled homogeneous and heterogeneous inhibitory networks of quadratic integrate-and-fire (QIF) neurons subject to Gaussian noise. The analysis is based on accurate extensive simulations and complemented by a mean-field description in terms of low-dimensional *next generation* neural mass models for heterogeneously distributed synaptic couplings. The asynchronous regime is observable at low noise and becomes unstable via a sub-critical Hopf bifurcation at sufficiently large noise. This gives rise to a coexistence region between the asynchronous and the clustered regime. The clustered phase is characterised by population bursts in the  $\gamma$ -range (30–120 Hz), where neurons are split in two equally populated clusters firing in alternation. This clustering behaviour is quite peculiar: despite the global activity being essentially periodic, single neurons display switching between the two clusters due to heterogeneity and/or noise.

## 1. Introduction

Since the pioneering studies of Winfree synchronisation phenomena in biological populations are usually addressed in the context of coupled oscillators [1]: synchronisation is associated to the emergence of a unique group of oscillators displaying a coherent dynamics [2]. Besides this phenomenology, one can observe also *clustering* phenomena, where the population breaks down in groups of elements displaying some sort of coherent evolution [3].

A paradigmatic complex system where these phenomena have been largely investigated are brain circuits. In this framework synchronisation among a group of neurons can induce the emergences of collective oscillations (COs) [4, 5]. In this context, the existence of inhibitory interactions is fundamental in order to promote fast collective oscillatory behaviours in several areas of the brain, in particular in the hippocampus and the neocortex [6, 7].

In real systems, and in particular in brain circuits, noise is unavoidable, therefore many analyses have been devoted to its influence on coherent dynamics. In particular, a common noise source can induce synchronisation and clustering phenomena, as shown for globally coupled or even uncoupled limit-cycle oscillators [8–11]. This peculiar synchronisation induced by common noise is referred in neurophysiology as ‘reliability’ [12].

But also for the case of independent noise, clustering phenomena have been reported for heterogeneous excitable systems with random coupling strengths for sufficiently broad distributions of the couplings [13]. Furthermore, clustering instabilities have been shown to affect the synchronised regime in homogeneous inhibitory networks of spiking neurons subject to additive noise [5].

In this paper, we analyse in details the role of noise in promoting a regime of coexistence among clustered and asynchronous dynamics in spiking neural networks. This is a particularly relevant regime, since brain dynamics in the awake state is typically characterised by an asynchronous activity of the neurons. However, oscillations in the  $\gamma$ -range (30–120 Hz) can occasionally emerge in relation with information processing, behaviour and learning [14–17]. In particular, we consider an inhibitory spiking neural network of quadratic integrate-and-fire (QIF) neurons [18] subject to Gaussian noise. The QIF model is quite general, since it represents the normal form describing the dynamics of all class I neurons in proximity to a saddle-node on a limit cycle bifurcation [19]. Furthermore, for heterogenous QIF networks exact low-dimensional mean-field (neural mass) models can be derived in terms of experimentally measurable quantities such as the population firing rate and the average membrane potential [20]. Recently, this approach has been extended to encompass extrinsic and endogenous sources of fluctuations (noise) leading to a hierarchy of low-dimensional neural mass models [21]. For his innovation with respect to classical neural mass models (e.g. the Wilson–Cowan one) this class of mean-field models has been termed *next generation* neural mass models (for the many possible applications in neural dynamics see [22]).

We will combine this mean-field analysis with accurate numerical simulations [23] to characterise at a macroscopic and microscopic level the coexisting dynamical regimes, as well as the stability of the asynchronous regime and the bifurcations associated to the emergence of the clustered state. To be more specific, the paper is organised as follows. Section 2 is devoted to the introduction of the QIF network model and the corresponding mean-field reduction methodology. The macroscopic and microscopic indicators employed to characterise the coherence and regularity of the neuronal dynamics are presented in section 2.3 together with a new stability criterion for the asynchronous state in finite networks inspired by the basin stability analysis [24]. The linear stability of the asynchronous solution of the neural mass models is analytically evaluated for Gaussian noise in section 3 and for Lorentzian noise in appendix A. The asynchronous and clustered dynamics are examined in details for heterogenous synaptic couplings in section 4.1 by combining accurate network simulations and neural mass results. Spectral analysis of the collective oscillations is reported in section 4.2 and a brief summary of the obtained results can be found in section 5. Finally, appendix B is devoted to the investigation of the network dynamics for homogenous synaptic couplings, appendix C reports details on the numerical simulations and in appendix D is discussed a possible criterion to select the optimal integration time step in noisy systems.

## 2. Models and indicators

### 2.1. Network model

We consider an inhibitory population of  $N$  globally coupled QIF neurons [25], whose membrane potential evolution is described by the following set of equations

$$\dot{V}_i = V_i^2 + \eta_i + \frac{J_i}{N} \sum_{j=1}^N \sum_n \delta(t - t_j^{(n)}) + \sqrt{2}\sigma \xi_i(t) \quad i = 1, \dots, N \quad (1)$$

where  $V_i$  is the membrane potential of the  $i$ th neuron,  $J_i < 0$  the inhibitory synaptic coupling strength and  $\eta_i$  the neuronal excitability. Whenever a membrane potential  $V_j$  reaches infinity a spike is emitted and  $V_j$  is reset to  $-\infty$ . The  $n$ th spike-time of neuron  $j$  is denoted by  $t_j^{(n)}$ .

Each neuron is subject to a common synaptic current  $J_i s(t)$ , where

$$s(t) = \frac{1}{N} \sum_{j=1}^N \sum_n \delta(t - t_j^{(n)}) \quad (2)$$

represents the activity of the network, as well as to an independent noise term of amplitude  $\sqrt{2}\sigma$ , where  $\xi_i(t)$  is a random Gaussian variable with  $\langle \xi_i(t) \xi_j(0) \rangle = \delta_{ij} \delta(t)$ .

In the absence of synaptic couplings and of external noise, a QIF neuron displays excitable dynamics for  $\eta_i < 0$ , while it behaves as an oscillator with period  $T_i = \pi / \sqrt{\eta_i}$  for positive  $\eta_i$ . For sake of simplicity we will assume homogenous excitabilities, by fixing  $\eta_i = \eta_0 = 4.2$ , thus all the uncoupled neurons will be supra-threshold.

In the following we will consider either heterogeneous quenched random couplings following a Lorentzian distribution (LD)

$$h(J_i) = \frac{1}{\pi} \frac{\Delta_J}{(J_i - J_0)^2 + \Delta_J^2} \quad (3)$$

or homogeneous couplings  $J_i \equiv J_0$ .

In order to characterise the macroscopic behaviour of the network two indicators will be essential to allow for a comparison with the mean-field formulation reported in the next subsection. One is the mean network activity  $s(t)$  (2) and the other the mean membrane potential, defined as follows

$$v(t) = \frac{1}{N} \sum_{i=1}^N V_i(t). \quad (4)$$

The identification of the spike-times is subject to some finite thresholding and the numerical integration of the set of stochastic differential Equations equation (1) is explained in details in C. The model is dimensionless, however to report the times (frequencies) in physical units, we will assume as a timescale for our dynamics  $\tau_m = 10$  ms, corresponding to the membrane time constant.

## 2.2. Next generation neural mass model

In the recent years, it has been shown that an exact low-dimensional mean-field formulation can be developed for fully coupled networks of heterogeneous QIF neurons, with Lorentzian distributed heterogeneities [20, 26–28]. This mean-field (neural mass) model describes the macroscopic dynamics of the network in the limit  $N \rightarrow \infty$  in terms of the mean membrane potential  $v$  (4) and the population firing rate  $r$ , which corresponds to the network activity  $s(t)$  (2). The main assumption of this approach is that the distribution of the membrane potentials is also Lorentzian at any time [20].

This *Lorentzian Ansatz* (LA) is violated if the neurons are randomly connected and/or in presence of noise. These more general cases can be treated by introducing a hierarchy of neural mass models taking in account the distortions to the LD of the membrane potentials [21]. Here we will briefly report the main steps to derive such mean-field formulation in the case of fully coupled inhibitory network of QIF neurons subject to additive noise.

In full generality, we can assume that both parameters  $\eta_i$  ( $J_i$ ) are distributed according to a LD  $g(\eta)$  ( $h(J)$ ) with median  $\eta_0$  ( $J_0$ ) and half width at half maximum (HWHM)  $\Delta_\eta$  ( $\Delta_J$ ). In the thermodynamic limit, the network dynamics equation (1) can be characterised in terms of the probability density function (PDF)  $p(V, t|\mathbf{x})$  with  $\mathbf{x} = (\eta, J)$ , which obeys the following Fokker–Planck equation (FPE):

$$\partial_t p(V, t|\mathbf{x}) + \partial_V [(V^2 + I_x) p(V, t|\mathbf{x})] = \sigma^2 \partial_V^2 p(V, t|\mathbf{x}), \quad (5)$$

where  $I_x \equiv \eta + Jr(t)$ . In [20] the authors assumed that in the absence of noise the solution of equation (5) converges to a LD for any initial PDF  $p(V, 0|\mathbf{x})$ , i.e. it becomes

$$p(V, t|\mathbf{x}) = \frac{a_x}{\left[ \pi \left( a_x^2 + (V - v_x)^2 \right) \right]}, \quad (6)$$

where  $v_x$  is the mean membrane potential and

$$r_x(t) = \lim_{V \rightarrow \infty} V^2 p(V, t|\mathbf{x}) = \frac{a_x}{\pi} \quad (7)$$

is the firing rate for the  $\mathbf{x}$ -subpopulation. The above LA joined with the assumption that the parameters  $\eta$  and  $J$  are independent and Lorentzian distributed lead to the derivation of exact low-dimensional neural mass models for globally coupled deterministic QIF networks [20].

Following what was done in [20] and extending it to noisy systems [21], one can introduce the characteristic function for  $V_x$ , i.e. the Fourier transform of its PDF, namely

$$\mathcal{F}_x(k) = \langle e^{ikV_x} \rangle = \text{P.V.} \int_{-\infty}^{+\infty} e^{ikV_x} p(V_x, t|\mathbf{x}) dV_x, \quad (8)$$

where P.V. indicates the Cauchy principal value. In this framework the FPE equation (5) can be rewritten as

$$\partial_t \mathcal{F}_x = ik [I_x \mathcal{F}_x - \partial_k^2 \mathcal{F}_x] - \sigma^2 k^2 \mathcal{F}_x. \quad (9)$$

Under the assumption that  $\mathcal{F}_x(k, t)$  is an analytic function of the parameters  $\mathbf{x}$  one can estimate the characteristic function averaged over the heterogenous population

$$F(k, t) = \int d\eta \int dJ \mathcal{F}_x(k, t) g(\eta) h(J)$$

and via the residue theorem the corresponding FPE, namely

$$\partial_t F = ik [H_0 F - \partial_k^2 F] - |k| D_0 F - \sigma^2 k^2 F; \quad (10)$$

where  $H_0 = \eta_0 + J_0 r$  and  $D_0 = \Delta_\eta + \Delta_J r$ .

For the logarithm of the characteristic function,  $\Phi(k, t) = \ln(F(k, t))$ , one obtains the evolution equation

$$\partial_t \Phi = ik [H_0 - \partial_k^2 \Phi - (\partial_k \Phi)^2] - |k| D_0 - \sigma^2 k^2. \quad (11)$$

In this context the LA amounts to  $\Phi_L = ikv - a|k|$ . By substituting  $\Phi_L$  in equation (11) for  $\sigma = 0$  one gets

$$\dot{v} = H_0 + v^2 - a^2, \quad \dot{a} = 2av + D_0, \quad (12)$$

which coincides with the two dimensional exact MF reported in [20] with  $r = a/\pi$ .

In order to consider deviations from the LD, the authors of [21] analysed the following general polynomial form for  $\Phi$

$$\Phi = -a|k| + ikv - \sum_{n=2}^{\infty} \frac{q_n |k|^n + ip_n |k|^{n-1} k}{n}. \quad (13)$$

and introduced the notion of complex *pseudo-cumulants*, defined as follows

$$W_1 \equiv a - iv, \quad W_n \equiv q_n + ip_n. \quad (14)$$

By inserting the expansion equation (13) in the equation (11) one gets the evolution equations for the pseudo-cumulants, namely:

$$\dot{W}_m = (D_0 - iH_0) \delta_{1m} + 2\sigma^2 \delta_{2m} + im \left( -m W_{m+1} + \sum_{n=1}^m W_n W_{m+1-n} \right), \quad (15)$$

where  $\delta_{ij}$  is the Kronecker delta function and for simplicity we assumed  $k > 0$ . It is important to notice that the time-evolution of  $W_m$  depends only on the pseudo-cumulants up to the order  $m + 1$ , therefore the hierarchy of equations can be easily truncated at the  $m$ th order by setting  $W_{m+1} = 0$ . As shown in [21] the modulus of the pseudo-cumulants scales as  $|W_m| \propto \sigma^{2(m-1)}$  with the noise amplitude, therefore it is justified to consider an expansion limited to the first few pseudo-cumulants.

In this paper, we will consider (15) up to the third order to obtain the corresponding neural mass model, i.e.

$$\dot{r} = 2rv + (\Delta_\eta + \Delta_J r + p_2) \pi^{-1} \quad (16a)$$

$$\dot{v} = \eta_0 + J_0 r - \pi^2 r^2 + v^2 + q_2 \quad (16b)$$

$$\dot{q}_2 = 2\sigma^2 + 4(p_3 + q_2 v - \pi p_2 r) \quad (16c)$$

$$\dot{p}_2 = 4(-q_3 + \pi q_2 r + p_2 v) \quad (16d)$$

$$\dot{q}_3 = 6(q_3 v - \pi r p_3 - q_2 p_2) \quad (16e)$$

$$\dot{p}_3 = 6(\pi r q_3 + p_3 v) + 3(q_2^2 - p_2^2), \quad (16f)$$

with the closure  $p_4 = q_4 = 0$ . The macroscopic variables  $r$  and  $v$  represent the population firing rate and the mean membrane potential, while the terms  $q_2, p_2, q_3, p_3$  take in account the dynamical modification of the PDF of the membrane potentials with respect to a Lorentzian profile. Besides the third-order neural mass models, we will also consider the second-order one, which can simply be obtained by considering equations (16a)–(16d) by setting  $q_3 = p_3 \equiv 0$

Since equation (16) is a set of deterministic ordinary differential equations, one can use standard numerical methods to integrate them. In particular, we employed a 4th order Runge–Kutta method [29]. The neural mass results will be compared with network simulations in the following and employed to initialise the network in an asynchronous state (see, e.g. sections 2.3.2 and appendix D).

## 2.3. Indicators

### 2.3.1. Macroscopic indicators

The evolution of the membrane potential of a neuron, in particular in the supra-threshold regime, can be interpreted as the rotation of the phase of an oscillator and many models have been derived by employing such an analogy. In terms of these phases the level of synchronisation of the oscillators (neurons) can be measured in terms of macroscopic order parameters that we will introduce in the following.

For the QIF model, the membrane potential  $V_i$  of the  $i$ th neuron is usually mapped in the phase  $\theta_i$  of an oscillator via the following transformation

$$\theta_i = 2 \arctan(V_i) \quad \theta_i \in [-\pi : \pi), \quad (17)$$

that leads from the QIF network equation (1) to the equivalent  $\theta$ -neuron network [18]:

$$\dot{\theta}_i = (1 - \cos(\theta_i)) + (1 + \cos(\theta_i)) \left( \eta_i + \frac{J_i}{N} \sum_{i=1}^N \sum_n \delta(t - t_i^{(n)}) + \sqrt{2}\sigma\xi_i(t) \right). \quad (18)$$

Unfortunately, the distribution of the phases  $P(\theta_i)$  is not uniform even for uncoupled neurons, since  $P(\theta_i) \propto 1/\dot{\theta}_i$ . This can therefore lead to apparent synchronisation phenomena in the  $\theta$ -space in noisy environments [30, 31].

In order to avoid such a problem, the phase  $\theta_i$  of the  $i$ th neuron at a certain time  $t$  can be obtained simply by interpolating linearly between the previous and the next spike time of the considered neuron, as follows

$$\theta_i(t) := 2\pi \frac{t - t_i^{(n)}}{t_i^{(n+1)} - t_i^{(n)}} - \pi \quad \text{with } t_i^{(n)} \leq t < t_i^{(n+1)}. \quad (19)$$

where  $t_i^{(n)}$  is the time at which the  $n$ th spike is emitted by  $i$ th neuron.

Now that the phases have been defined, we can introduce suitable order parameters to measure the level of phase synchronisation in the network [32–36], in particular we consider the so-called *Kuramoto–Daido order parameters*

$$Z_k = z_k e^{i\Psi_k} = \frac{\sum_{n=1}^N e^{ik\theta_n}}{N}, \quad (20)$$

where  $Z_k$  is a complex number and  $z_k$  and  $\Psi_k$  are the corresponding modulus and phase. For  $k=1$  the usual Kuramoto order parameter [32] is recovered. For a network of  $N$  oscillators one expects  $z_1 \simeq \mathcal{O}(1/\sqrt{N})$  in the asynchronous regime and  $z_1$  will be finite (one) for a partially (fully) synchronised state. Unfortunately,  $z_1$  is also exactly zero when the oscillators are equally divided in 2 perfectly synchronised clusters in anti-phase. To characterise regimes presenting  $k$  clusters, Daido [33] introduced the parameters  $Z_k$ . Indeed,  $z_k$  will be one whenever the system presents  $k$  clusters equally spaced in phase and equally populated, while  $z_k$  will approach zero for a sufficiently large network if the phases are evenly distributed over the whole interval.

To denote that the order parameters are estimated by employing the phases defined in terms of the spiking times as in equation (19) we will use a super-script ( $s$ ), while the lack of a super-script will denote the use of the phases defined as in equation (17).

In the mean-field framework previously introduced in section 2.2,  $Z_k$  can be obtained as follows [37]

$$Z_k = z_k e^{i\Psi_k} = \left( 1 - \frac{W_2}{2} (\partial_{W_1})^2 + \frac{W_3}{3} (\partial_{W_1})^3 + \frac{W_2^2}{8} (\partial_{W_1})^4 + \dots \right) \left( \frac{1 - W_1}{1 + W_1} \right)^k. \quad (21)$$

Note that the corrections obtained from the higher order pseudo cumulants  $W_j$ , i.e. with  $j > 3$ , should be negligible. In absence of noise and for the usual Kuramoto order parameter  $Z_1$  this reduces to the following conformal transformation

$$Z_1 = \frac{1 - W_1}{1 + W_1}, \quad (22)$$

as shown in [20].

Another macroscopic indicator able to distinguish asynchronous regimes from oscillatory ones characterised by a partial synchrony of the neurons is the variance  $\Sigma_v$  of the mean membrane potential  $v$  estimated over a certain time window  $T_w$ . This quantity is expected to be vanishing small  $\Sigma_v \simeq \mathcal{O}(1/N)$  in the asynchronous regime and finite whenever COs are present.

In order to identify the asynchronous and partially synchronised regime, since these are characterised by definitely different values of  $\Sigma_v$ , we can define a threshold value  $S_\theta$  and whenever  $\Sigma_v < S_\theta$  ( $\Sigma_v \geq S_\theta$ ) the dynamics will be identified as asynchronous (partially synchronised). The threshold value  $S_\theta$  is usually chosen as the mean of the values measured in the asynchronous and partially synchronised regimes, however the identification of the regimes is quite insensitive to the exact value of  $S_\theta$ .

Also the Kuramoto–Daido order parameter can be employed for this discrimination, and as we will see in the following for the examined dynamics the most suitable indicator will be  $z_2^s$ .

### 2.3.2. Stability criterion

The considered model exhibits in a certain parameter interval a region of coexistence of two different dynamical regimes: an asynchronous and a partially synchronous one. Our goal is to quantify the stability of the asynchronous regime for the finite network by varying the noise intensity. Therefore, we have introduced the following criterion inspired by the basin stability criterion [24], which has been applied in many different contexts [38–42].

The main idea is to consider a solution of a system, perturb this solution several times with a magnitude that is given by a parameter and let the dynamics evolve each time. Then one measures the fraction of how often the system evolves back to a desired solution. Here, we proceed as follows: we initialise the values of the membrane potentials  $\{V_i\}$  according to

$$V_i = \tan\left(\frac{\pi(2i - N - 1)}{2(N + 1)}\right) \gamma \Delta_V + V_0 \quad i = \{1, 2, \dots, N\}, \quad (23)$$

with  $V_0 = v^*$  and  $\Delta_V = \pi r^*$ , where  $(v^*, r^*)$  are the fixed point solution of the third-order neural mass model equation (16). Note that for  $\gamma = 1$  equation (23) will result in the Lorentzian distribution that is expected for an asynchronous regime at equilibrium, while the extreme case  $\gamma = 0$  fixes all the membrane potentials  $V_i \equiv V_0$ , i.e. it results in a fully synchronised initial state.

For different values of the parameter  $\gamma \leq 1$  we simulate the system for a time  $T_t$ , after which we verify whether the system is asynchronous or partially synchronised. For each value of  $\gamma$  we repeat this procedure  $M$  times for different noise realisations and count how many times  $M_c$  the system exhibits its asynchronous state after the integration time  $T_t$ . Thus, we can measure the stability of the asynchronous state of the chosen configuration via the following indicator

$$\rho = \frac{M_c}{M}. \quad (24)$$

A completely stable (unstable) asynchronous regime will correspond to  $\rho = 1$  ( $\rho = 0$ ) for any value of  $\gamma$ . However, in general  $\rho$  will be a function of  $\gamma$ . In the bistable regime, by decreasing the  $\gamma$  value one will eventually observe a transition towards the partially synchronised regime. Thus, the value of  $\gamma$  where this ‘transition’ happens is a measure of the stability of the bistable system.

### 2.3.3. Characterisation of irregular spiking

As we will show in the following, the partially synchronised state is characterised by two clusters of neurons firing in anti-phase. Furthermore, the neurons in each cluster do not remain in the same cluster over long time periods. Instead they tend to switch from one cluster to the other, despite the collective dynamics being always characterised by two clusters of neurons firing in alternation. Therefore the usual behaviour for a neuron is to fire in correspondence with every second neuronal burst, but with irregularities in this repetition. We want to introduce a measure of these irregularities in the sequence of spikes of the neurons.

In order to develop this measure we store the sets  $\mathcal{S} = [s_1 = (t_1, i_1), s_2 = (t_2, i_2), s_3 = \dots]$  of firing times and firing neurons in the network for a certain time interval, where  $t_j$  is the firing time and  $i_j \in [1, \dots, N]$ , the index of the firing neuron. Moreover, we also store the bursting times  $b_k$  at which the neuronal bursts occur. These are identified by the maxima in the population firing rate  $r$ . As a convention we define the burst  $k$  as the collection of all the spiking events occurring within the time interval

$$B_k = \left[ \frac{b_{k-1} + b_k}{2}, \frac{b_k + b_{k+1}}{2} \right). \quad (25)$$

thus the spike  $s_m$  is emitted within the burst  $k$  if  $t_m \in B_k$ .

The regular behaviour for a 2 cluster state would be that a neuron, which fires within the burst  $k$ , would emit its next spike within the burst  $k + 2$ . To analyse the eventual irregularity of the individual neurons we create a ordered list  $\mathcal{K}_i = \{k_m^{(i)}\}$  reporting the bursts within which the considered neuron  $i$  has fired during the observation time interval  $T$ . The first two bursts  $k = 0$  and  $k = 1$  are employed to identify if the neuron

belongs to the first or second cluster, i.e.  $k_0^{(i)} = 1$  ( $k_0^{(i)} = 0$ ) if the spike of neuron  $i$  occurred within  $B_1$  ( $B_0$ ). Then, for each neuron we introduce a counter  $E_i$  of ‘early spikes’ in the following way: We go through the list  $\mathcal{K}_i$  of bursts to which neuron  $i$  has contributed and we increment  $E_i$  by one each time  $k_{n+1}^{(i)} - k_n^{(i)} < 2$ . If we had a total of  $\mathcal{B}$  bursts in the considered time interval  $T$ , then the fraction of spikes that have been emitted too early by the neuron  $i$  is

$$\lambda_i^E = \frac{E_i}{\mathcal{B}}. \quad (26)$$

In particular if a neuron would fire during each burst we will have  $\lambda_i^E = 1$ .

Similarly, the fraction of ‘late delivered spikes’ can be calculated by using a second counter  $L_i$  that is incremented by one each time  $k_{n+1}^{(i)} - k_n^{(i)} > 2$ , which leads to define the following fraction of late spiking neurons

$$\lambda_i^L = \frac{L_i}{\mathcal{B}}. \quad (27)$$

Note that  $\lambda_i^L \leq \frac{1}{3}$  due to its definition, since the counter is incremented whenever  $k_{n+1}^{(i)} - k_n^{(i)}$  is at least 3.

In summary, the percentage of times the spikes occur outside of the expected time-frames, i.e. the percentage of irregular spikes, is

$$\lambda_i = \frac{E_i + L_i}{\mathcal{B}} = \lambda_i^L + \lambda_i^E. \quad (28)$$

The number of neurons for which  $\lambda_i = 0$  until the time  $t$  define *the surviving neurons*, i.e. those which fire regularly every 2 bursts as expected. The fraction of surviving neurons  $S(t)$  until the time  $t$  can be defined as

$$S(t) = \frac{\sum_{i \in \mathcal{N}} \delta_{0, \lambda_i(t)}}{\mathcal{N}}, \quad (29)$$

where  $\delta$  is the Kronecker delta, and  $\mathcal{N}$  is the number of non-silent neurons. The silent neurons should be removed from the count, since one always has  $\lambda_i = 0$  for those neurons: a neuron that never spikes obviously does not have any associated spike time in an unexpected time interval. For our analysis we considered  $T = 55$  s.

The survival probability  $S(t)$  is usually defined as [43] :

$$S(t) = 1 - F(t);$$

where  $F(t) = \int_0^t f(t') dt'$  is the cumulative distribution function and  $f(t)$  the PDF of the neuronal survival times, i.e. the time until which the considered neuron fires regularly once every two bursts.

### 3. Linear stability analysis of the asynchronous state

In this section we analyse the stability of the asynchronous regimes within the neural mass formulation. For the neural mass model equation (16), the asynchronous states correspond to fixed point solutions  $(r^*, v^*, q_2^*, p_2^*, q_3^*, p_3^*)$ . In particular, we will study the stability of these solutions by considering the linearisation of equation (16) in proximity of the considered fixed points, namely

$$\delta \dot{r} = 2(v^* \delta r + r^* \delta v) + (\Delta_J \delta r + \delta p_2) \pi^{-1} \quad (30a)$$

$$\delta \dot{v} = (J_0 - 2\pi^2 r^*) \delta r + 2v^* \delta v + \delta q_2 \quad (30b)$$

$$\delta \dot{q}_2 = 4(\delta p_3 + q_2^* \delta v + v^* \delta q_2 - \pi p_2^* \delta r - \pi r^* \delta p_2) \quad (30c)$$

$$\delta \dot{p}_2 = 4(-\delta q_3 + \pi q_2^* \delta r + \pi r^* \delta q_2 + p_2^* \delta v + v^* \delta p_2) \quad (30d)$$

$$\delta \dot{q}_3 = 6(q_3^* \delta v + v^* \delta q_3 - \pi r^* \delta p_3 - \pi p_3^* \delta r - q_2^* \delta p_2 - p_2^* \delta q_2) \quad (30e)$$

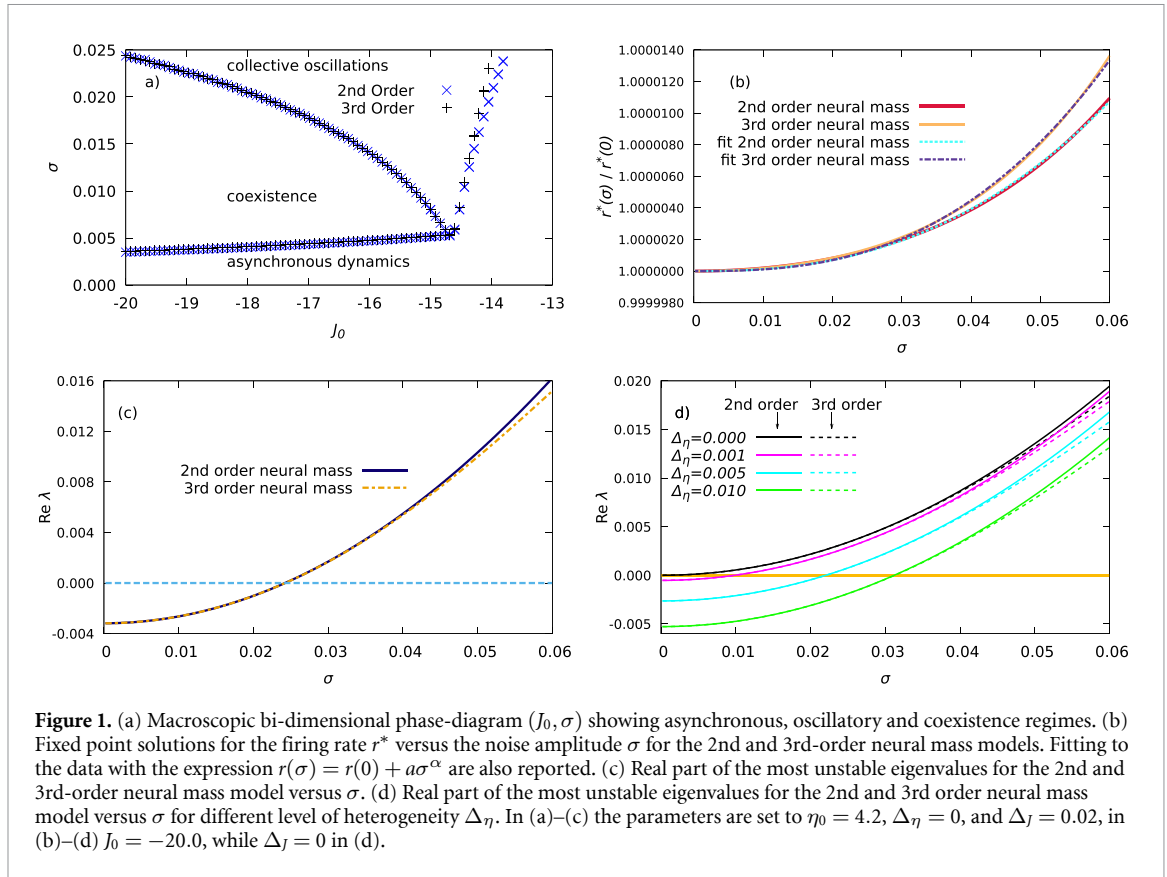
$$\delta \dot{p}_3 = 6(\pi r^* \delta q_3 + \pi q_3^* \delta r + p_3^* \delta v + v^* \delta p_3 + q_2^* \delta q_2 - p_2^* \delta p_2). \quad (30f)$$

#### 3.1. Deterministic case

Let us start from the case in absence of noise. In this case the mean-field equations reduce to the exact formulation reported in [20]

$$\dot{r} = 2rv + (\Delta_\eta + \Delta_J r) \pi^{-1} \quad \text{and} \quad \dot{v} = \eta_0 + J_0 r - \pi^2 r^2 + v^2. \quad (31)$$





The fixed point solutions can be obtained by solving the following equations

$$v^* = -\frac{\Delta_\eta}{2\pi r^*} - \frac{\Delta_J}{2\pi} \quad (32)$$

$$\pi^2 (r^*)^4 - J_0 (r^*)^3 - \left( \eta_0 + \frac{\Delta_J^2}{4\pi^2} \right) (r^*)^2 - 2 \frac{\Delta_J \Delta_\eta}{4\pi^2} r^* - \frac{\Delta_\eta^2}{4\pi^2} = 0 \quad (33)$$

for the parameter values considered in this paper, namely inhibitory coupling  $J_0 = -20$ ,  $\eta_0 = 4.2$  and  $\Delta_J = 0.02$  and  $0 \leq \Delta_\eta \leq 0.30$  the system exhibits 2 complex conjugate and 2 real solutions. Among the real ones only one corresponds to a positive firing rate  $r^*$  and is therefore physically acceptable.

The stability of such a solution can be obtained by analysing the linear evolution  $(\delta r(t), \delta v(t)) = e^{\lambda t} (\delta r(0), \delta v(0))$  in proximity of the physical fixed point solutions  $(r^*, v^*)$ . This amounts to solving second order characteristic equations for the eigenvalue problem associated to equation (30) with  $p_2 = q_2 = p_3 = q_3 = 0$ , which gives the following result

$$\lambda_{\pm} = \left( 2v^* + \frac{\Delta_J}{2\pi} \right) \pm \sqrt{2J_0 r^* - 4\pi^2 (r^*)^2 + \frac{\Delta_J^2}{4\pi^2}}. \quad (34)$$

For the chosen values of the parameters the square root in equation (34) is always purely imaginary. Therefore the fixed point is a focus and, when inserting equation (32), the real part of the eigenvalues is simply given by

$$Re\lambda = -\frac{\Delta_\eta}{\pi r^*} - \frac{\Delta_J}{2\pi}. \quad (35)$$

The focus is always stable, apart from the fully homogenous situation  $\Delta_\eta = \Delta_J = 0$  in which case it becomes marginally stable. The heterogeneities tend to stabilise the focus solutions. Therefore, even in the case of homogeneous coupling  $\Delta_J = 0$ , a small heterogeneity in the excitabilities measured by  $\Delta_\eta$  is sufficient to render the fixed point stable. This can be seen in the following for  $\sigma = 0$  in figure 1(d).

### 3.2. Gaussian noise

In presence of additive Gaussian noise of amplitude  $\sigma$ , we always observe a stable focus for sufficiently small  $\sigma$ . However, these fixed points solutions get destabilised via a Hopf bifurcation at sufficiently large noise giving rise to collective oscillations. This can be seen in figure 1(a), where we report a two dimensional phase-diagram in the plane  $(J_0, \sigma)$  obtained via quasi-adiabatic simulations of the 2nd and 3rd order neural mass models for  $\eta_0 = 4.2$ ,  $\Delta_\eta = 0$ , and  $\Delta_J = 0.02$  (for more details see appendix C). In particular, for  $J_0 < J_0^{(c)} \simeq -14.6$  one observes a coexistence region for asynchronous (fixed point) and oscillatory solutions bounded at large  $\sigma$  values by a sub-critical Hopf bifurcation and at low  $\sigma$  values by a saddle node bifurcation of limit cycles [21]. At larger  $J_0 > J_0^{(c)}$  one has a direct transition from a fixed point to COs mediated by a super-critical Hopf bifurcation and no more coexistence of these solutions.

Since we are interested in the coexistence regime, in the following we will consider  $J_0 < J_0^{(c)}$  (in most of the cases  $J_0 = -20$ ). For these parameter values, the effect of noise is to induce an increase of the firing rate  $r^*(\sigma)$  with respect to the case in absence of noise  $r^*(0)$ . In particular, the correction to the deterministic solution can be written as  $r^*(\sigma) \simeq r^*(0) + a\sigma^\alpha$ . For the parameters previously specified, one obtains  $\alpha \simeq 2.5$  for the 2nd-order neural mass model, while the growth is even faster for the third-order model with  $\alpha \simeq 2.7$ , as evident from figure 1(b).

To analyse the stability of the fixed points we have identified the corresponding eigenvalues by solving the associated characteristic polynomial, that can be of the 4th (6th) order depending if we consider the neural mass model to the 2nd (3rd) order. The linear stability analysis reveals that the 4 eigenvalues for the 2nd order neural mass are two complex conjugate pairs, whose real parts are definitely negative for  $\sigma = 0$  and  $\Delta_\eta$  and/or  $\Delta_J$  not zero, as evident from equation (35).

As shown in figure 1(c) for homogeneous currents ( $\Delta_\eta = 0$ ) and heterogenous synaptic couplings ( $\Delta_J = 0.02$ ), noise destabilises the fixed point, since it leads to an increase of the real part of the maximal eigenvalues. In particular, these two eigenvalues can cross the zero axis at a critical noise amplitude  $\sigma_H$ . Thus indicating that the fixed point solution becomes unstable via a Hopf bifurcation giving raise to COs. For the case shown in figure 1(c) we have  $\sigma_H \simeq 0.0243$ . The third order model displays 3 pairs of complex conjugates eigenvalues, however the fixed point loses stability exactly at the same  $\sigma_H$  value via a Hopf bifurcation (see figure 1(c)).

The effect of the noise on the stability of the foci is analogous for a network with homogenous couplings ( $\Delta_J = 0$ ) and heterogeneous currents  $\Delta_\eta > 0$ , as shown in figure 1(d).

## 4. Numerical results

In this section we will analyse and characterise the clustering transition induced by noise. In particular, we will focus on heterogenous couplings, where we fix  $\Delta_J = 0.02$ , in this case we will compare the results obtained within the mean-field approach with network simulations. In appendix B, we will examine the homogenous situation, where  $\Delta_J = 0$ , by relying only on network simulations. Section 4.2 will be devoted to the characterisation of the  $\gamma$ -oscillations emerging in the oscillatory regime for heterogenous and homogenous synaptic couplings. If not specified otherwise we fix the parameters to the following values  $J_0 = -20$ ,  $\eta_0 = 4.2$  and  $\Delta_\eta = 0$ , and we consider an inhibitory network of size  $N = 200\,000$  subject to Gaussian additive noise.

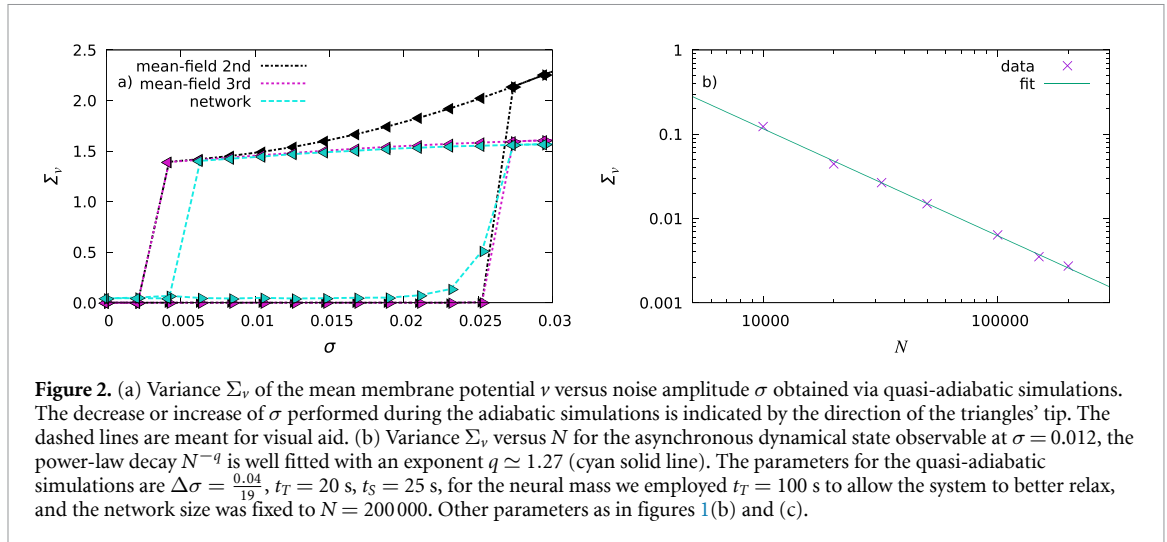
### 4.1. Heterogeneous synaptic couplings

In section 3.2 we have shown that in the mean-field formulation the asynchronous regime remains stable up to a noise of amplitude  $\sigma_H \simeq 0.0243$ , where it destabilises via a Hopf bifurcation. In this subsection we will characterise such a transition and the observed regimes in full details.

#### 4.1.1. The clustering transition

In order to understand if the transition is super- or sub-critical, we perform simulations by varying quasi-adiabatically the noise amplitude  $\sigma$  (for details see appendix C) and by measuring for each value of  $\sigma$  the variance  $\Sigma_v$  of the mean membrane potential.

As shown in figure 2(a), for the 2nd and 3rd order neural mass models we observe that starting from  $\sigma = 0$  and by increasing the noise amplitude, the variance  $\Sigma_v$  remains zero until a value near  $\sigma_H$  is reached, as expected for a constant mean membrane potential ( $v = v^*$ ). Afterwards it jumps to some finite value due to the emergence of COs. Once the noise amplitude reaches  $\sigma = 0.03$  the quasi-adiabatic simulations are then continued by decreasing  $\sigma$  in steps of  $\Delta\sigma$ . In this case  $\Sigma_v$  stays finite down to values  $\sigma_{SN} \simeq 0.004$  and then at even smaller value of  $\sigma$  returns to zero. This scenario is typical for a sub-critical Hopf bifurcation, characterised by the coexistence of oscillatory and stationary behaviours in the range  $\sigma \in [\sigma_{SN}, \sigma_H]$ . In



particular, at  $\sigma_{SN}$  one expects that the oscillatory solution will disappear via a saddle-node bifurcation of limit cycles.

The network simulations agree quite well with those of the 3rd order neural mass model, apart some finite-size effects that imply finite values  $\mathcal{O}(1/N)$  for  $\Sigma_v$  even in the asynchronous regime and a backward transition from the oscillatory to the asynchronous regime occurring at a larger noise amplitude, namely  $\sigma \simeq 0.006$ , instead that at  $\sigma_{SN}$ . The scaling of the variance  $\Sigma_v$  with  $N$  is reported in figure 2(b), the observed power-law decrease is even faster than expected from the central limit theorem for a purely asynchronous regime. This is probably due to the fact that the macroscopic fixed point is in this case a focus, therefore displaying transient oscillations that are excited by the finite size fluctuations, whose amplitude decrease faster than  $1/N$ .

In contrast, the 2nd order neural mass model displays clear differences with the 3rd order one and the network simulations in the oscillatory regime for  $\sigma > 0.01$  (see black triangles in figure 2(a)). This is probably due to an instability of the 2nd order model at large noise amplitudes. Here, we have considered very large network sizes  $N = 200\,000$  to compare with the mean field results. The coexistence regime is observable also for smaller system sizes, down to  $N = 10\,000$ , however it is limited to a smaller interval of noise values due to the destabilising effect of finite size fluctuations.

#### 4.1.2. Coexisting solutions

Let us now examine the macroscopic properties of the asynchronous and clustered regimes in the coexistence region in more detail. In order to gain some insight we report the mean membrane potential  $v$  versus time for the two regimes at  $\sigma = 0.00842$  in figures 3(a) and (d). In the asynchronous state  $v$  is exactly constant for the neural mass simulations, while it displays small erratic fluctuations when obtained from network simulations. This is due to the fact that the stable fixed point is a focus, therefore the presence of finite-size fluctuations excites continuously relaxation oscillations towards the focus. As shown in figure 3(d)  $v(t)$  is periodically oscillating in the clustered regime and in this case the network simulations agree quite well with the neural mass results obtained for both 2nd and 3rd order models.

It is interesting to examine the level of synchronisation in the two regimes as measured by the Kuramoto order parameters  $z_1$  and  $z_2$ , see figures 3(b), (c) and (e), (f). In the asynchronous state shown in panels (b) and (c) the neural mass results give a finite value for  $z_1$  and  $z_2$ , while for an asynchronous regime one would expect zero values in the mean-field limit. The values of  $z_1$  and  $z_2$  obtained by the network simulations oscillate in an irregular fashion slightly around the mean-field value. For what concerns the clustered regime, the order parameters reveals periodic oscillations with the same period as  $v(t)$  and significant amplitudes. In this case the neural mass and the network results essentially coincide as shown in panels (e) and (f).

In order to understand the reason why  $z_1$  and  $z_2$  have a finite value in the asynchronous regime let us investigate the distribution of the phases as defined in equation (17). Histograms of these phases are shown in figure 4 for the asynchronous and clustered regime. In the asynchronous regime the phases are not equally distributed in  $[-\pi; +\pi]$  as expected they exhibit a peak around zero instead. This peak is much more pronounced in the clustered regime, but there is no evidence of the two clusters. This is due to the fact that the phase definition equation (17) is related to the membrane potential value, whose values also displays similar unimodal PDFs (see the supplementary material for animations of the phase histograms from

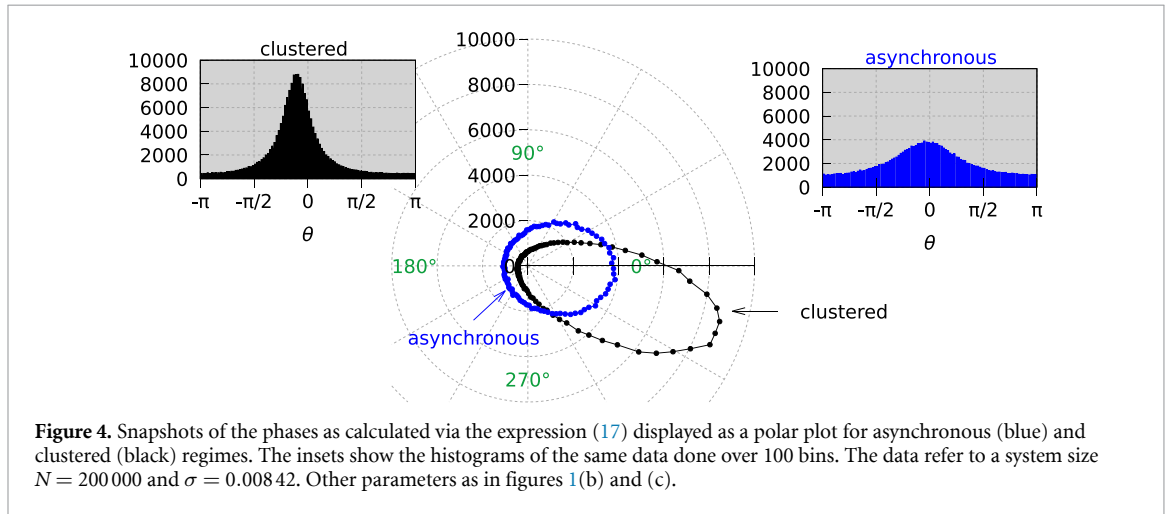
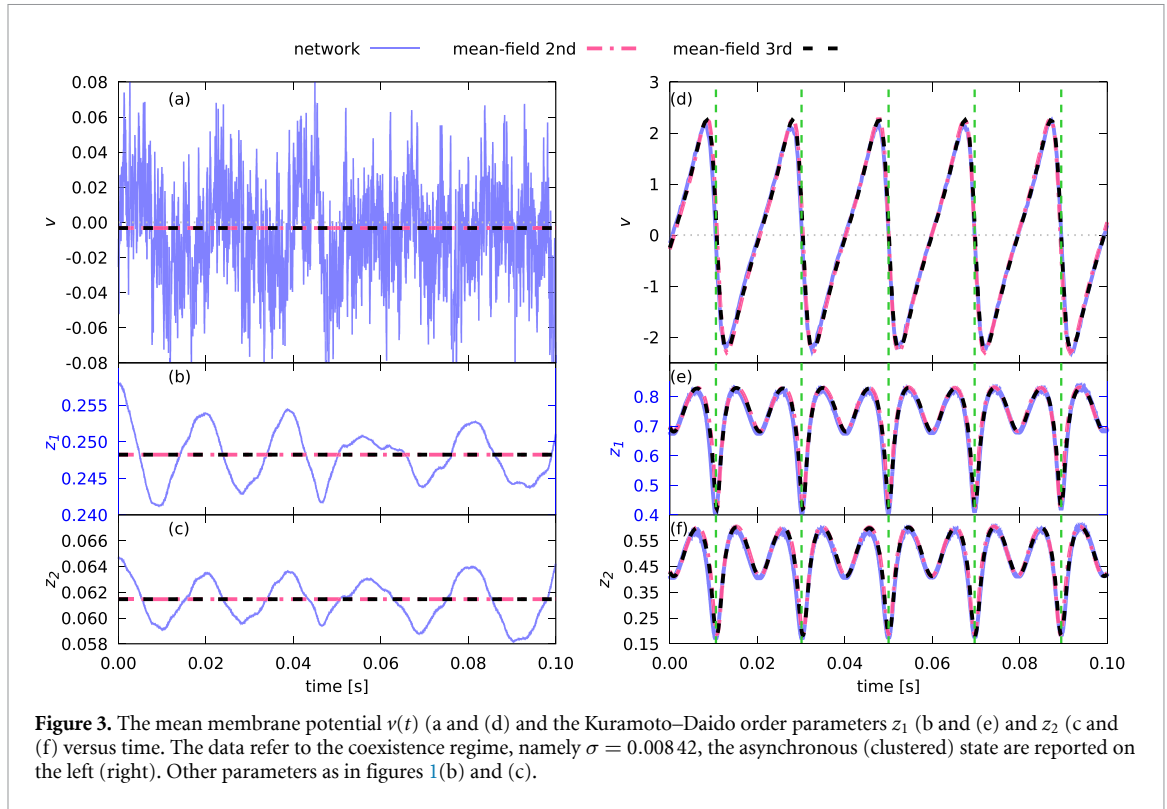
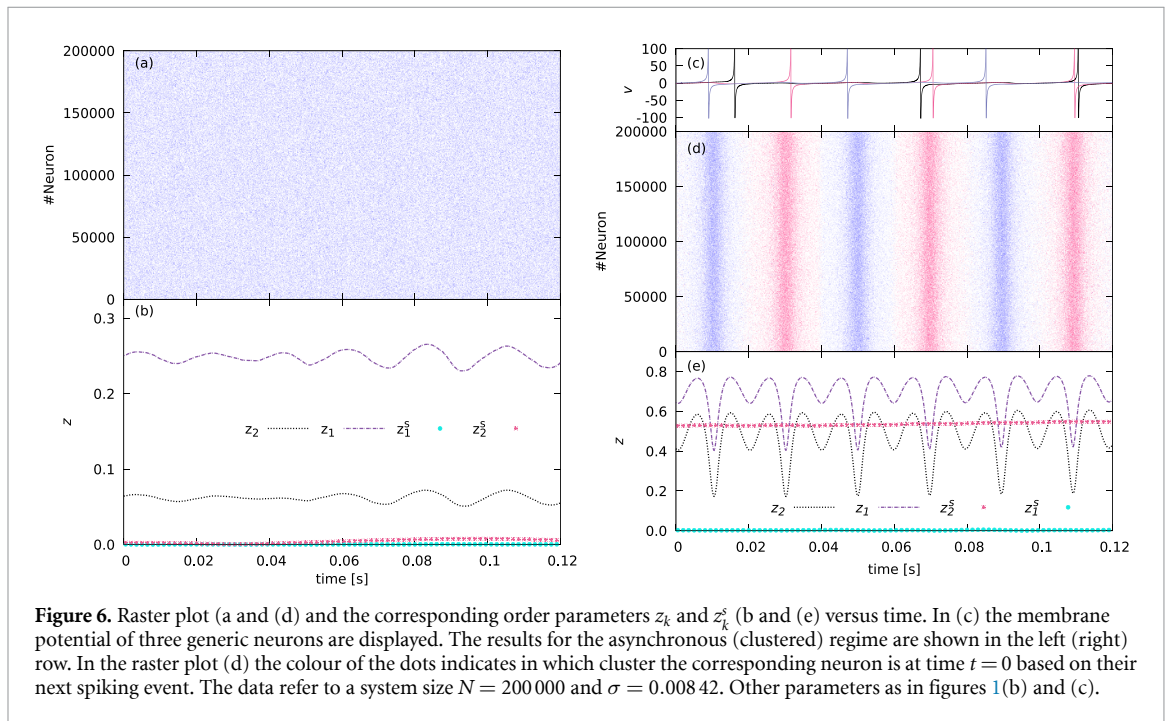
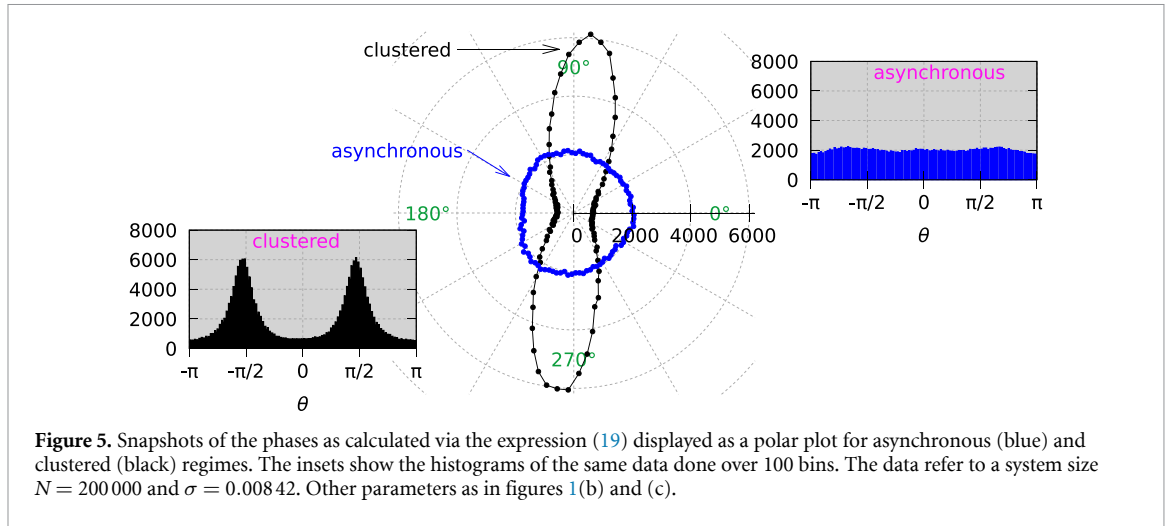


figure 4 and the corresponding membrane potential histograms), and not to the firing time of the corresponding neuron, thus making this phase unsuitable to characterise the observed neural dynamics.

Let us now consider the distributions of the phases as obtained by the firing times via the definition equation (19) for the asynchronous and oscillatory regimes. The results are shown in figure 5. Note that animations of these histograms can be found in the Supplementary Material. In the asynchronous case, as expected, the phases are uniformly distributed. The results for the oscillatory regimes reveal that the neurons are arranged in two clusters in phase opposition (at a distance  $\pi$ ) from one another. In this case we expect that the Kuramoto order parameter  $z_1^s$  ( $z_2^s$ ) should be zero (order one) since the 2 clusters are in phase opposition.

To get some more insight on these two dynamical states, we will examine the raster plots as a measure of the microscopic network activity joined to the traces of the Kuramoto–Daido order parameters  $z_k$  and  $z_k^s$  for the macroscopic counterpart. These are shown in figure 6.

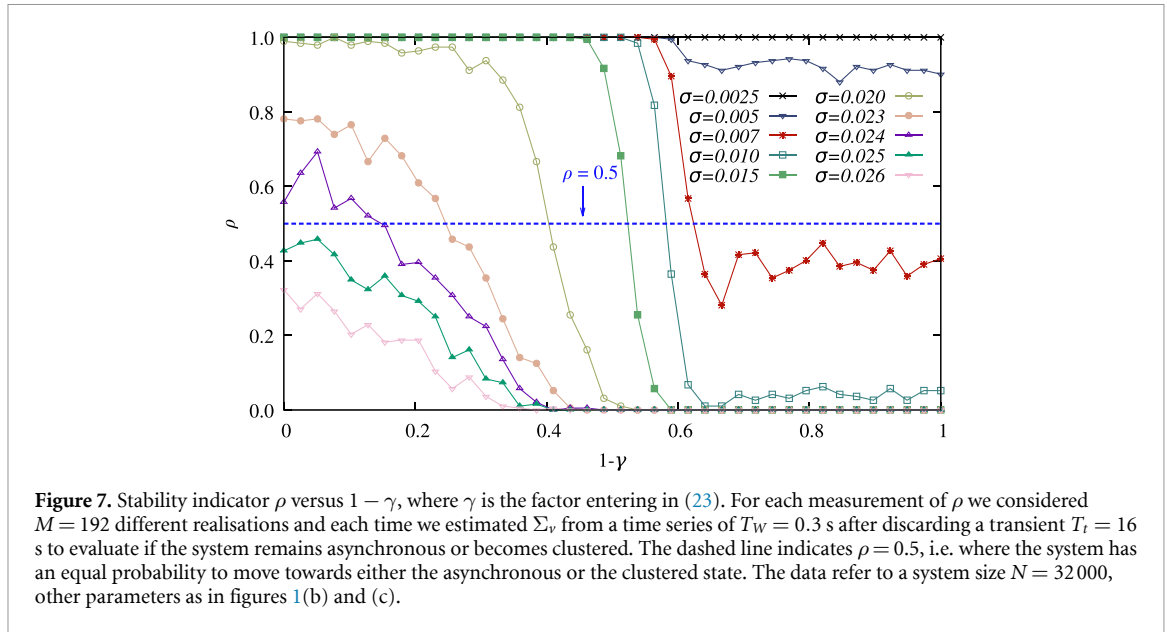
In the asynchronous regime, the raster plot in panel (a) does not display any structure and the corresponding Kuramoto–Daido order parameters  $z_k^s$ ,  $k = 1, 2$  estimated by the firing-times are of  $\mathcal{O}(1/\sqrt{N})$  as expected (see panel (b)). As shown in panel (b) the values of  $z_1$  and  $z_2$  are instead definitely finite due to



the fact that the phases obtained via the transformation equation (17) are not uniformly distributed, even in this regime.

In the clustered regime the raster plot (shown in panel (d)) reveals bursts of activity of the neurons interrupted by a low activity phase. In each population burst roughly 50% of the neurons participate. In the raster plot, the spiking times are visualised by red and blue coloured dots based on which cluster the corresponding neuron belonged at time  $t = 0$ , for which we used the next spiking event of the corresponding neuron. In the time window reported in panel (d) the clusters are apparently stable, however on a longer run the two ensembles will mix up completely despite the macroscopic dynamics remaining always characterised by two equally populated clusters. To exemplify these behaviours in panel (c) the membrane potential traces for 3 characteristic neurons have been reported: the red (blue) neuron is always firing within the red (blue) burst, while the black one is initially firing within the blue burst but then it skips 2 population bursts and finally joins the red burst.

In panel (e) we report the corresponding Kuramoto–Daido order parameters versus time, the parameters  $z_1$  and  $z_2$  display a periodic behaviour and attain the minimum value whenever a burst occurs, due to the repulsive nature of the couplings. On the other hand,  $z_1^s$  stays always close to zero as expected for two phase clusters in phase opposition, while  $z_2$  has a constant finite value larger than 0.5 indicating that the composition of the clusters is stable in time. The results reported in this Paragraph refer to a specific choice



of the noise amplitude,  $\sigma = 0.00842$ , however analogous results can be found in the whole coexistence region, as we have verified (results not shown).

#### 4.1.3. Stability of the asynchronous regime

In this Paragraph we will analyse the stability of the asynchronous state for increasing noise amplitude. For this we will employ the stability indicator  $\rho = \rho(\gamma)$  introduced in equation (24) as a function of the parameter  $\gamma$  controlling the initial distribution of the membrane potentials according to equation (23). The value  $\gamma = 1$  ( $\gamma = 0$ ) corresponds to an initialisation of the neurons with membrane potentials distributed according to the LD expected for the asynchronous case (with identical values of the membrane potentials  $V_0$ ).

We have estimated the stability indicator  $\rho(\lambda)$  for a system size  $N = 32\,000$  (due to cpu limits) and the results are reported in Figure 7 for different noise amplitudes. For the noise amplitude  $\sigma = 0.0025$ , which is smaller than  $\sigma_{SN} \simeq 0.004$  and therefore outside the coexisting region, we observe that the asynchronous state is stable for any  $\gamma$ -values, as expected. For larger noise amplitude  $\sigma > \sigma_{SN}$ , large perturbation of the asynchronous distribution, as measured by  $1 - \gamma$ , can induce transitions towards the clustered regime with some finite probability.

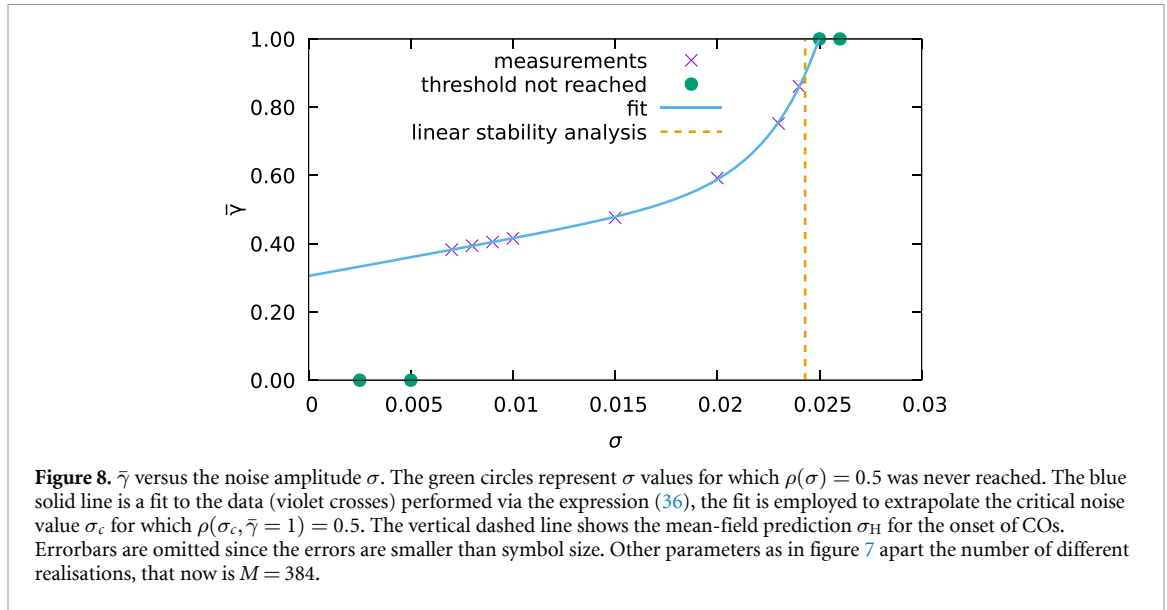
At noise amplitudes  $\sigma \geq 0.015$ , for sufficiently synchronised initial conditions, namely  $\gamma < 0.4$ , the system has a probability of almost 100% to leave the asynchronous state, thus indicating a clear coexistence of the 2 regimes. For  $\sigma \geq 0.023$  (i.e. in proximity of the Hopf bifurcation identified in the mean-field formulation  $\sigma_H = 0.0243$ ) the probability to stay in the asynchronous case is smaller than 100% even for the unperturbed initial conditions, corresponding to  $\gamma = 1$ , in this case we expect that by simulating for a longer time period  $T_t$  we would actually measure  $\rho = 0$ .

In order to identify the critical noise amplitude above which the asynchronous state is unstable, we measure the value  $\bar{\gamma}$  for which  $\rho(\bar{\gamma})$  crosses  $\frac{1}{2}$  for various noise amplitudes  $\sigma$ . Thus, this indicates that for  $\gamma = \bar{\gamma}$  one has 50% of probability to end in the asynchronous or in the clustered state. For this we estimated the indicator with more precision in proximity of  $\rho(\bar{\gamma}) \approx \frac{1}{2}$ . To this end we considered  $M = 384$  realisations of the initial perturbed state for each value of  $\gamma$ , and we estimated via an interpolation the value  $\bar{\gamma}$ . In particular, we expect that the standard deviation of  $\rho(\gamma)$  will be maximal at exactly one half, therefore we fitted such standard deviation to a Gaussian curve for different  $\gamma$  value and we extrapolated the value  $\bar{\gamma}$  where the curve attains its maximum.

In figure 8 we show the obtained values  $\bar{\gamma}$  as a function of noise amplitude  $\sigma$  (violet crosses), we observe that  $\bar{\gamma}$  grows with the noise amplitude and approaches the value  $\bar{\gamma} = 1$ . To identify the critical noise amplitude  $\sigma_c$  above which the system always ends up in the clustered regime for any  $\gamma$  value we have fitted the numerical data with this function:

$$f(\sigma) = 1 + a \left( 1 - e^{b(\sigma - \sigma_c)} \right) + c(\sigma - \sigma_c). \quad (36)$$

By excluding from the fit the data where the threshold value  $\rho = 0.5$  was not reached (green points) we obtain the following parameter values  $a = -0.42(1)$ ,  $b = 376(28)$ ,  $c = 10.9(8)$  and  $\sigma_c = 0.02498(6)$ . As you can see



the fit works pretty well. The extrapolated critical value of the noise is in quite good agreement with the mean-field result obtained from the linear stability analysis of the asynchronous state that indeed was  $\sigma_H = 0.0243$ , the difference on the third significant digit can be due to finite-size and nonlinear effects.

In summary the new method here introduced to study the stability of the asynchronous regime works reasonably well when compared with the linear stability analysis, that in the present case is feasible due to the existence of low-dimensional mean-field formulations, but usually in a high dimensional network is quite difficult to implement. Therefore, this new method can represent an useful alternative to the linear stability analysis and it can find applications in many complex network systems. Furthermore, it gives also information concerning the basins of attraction of the two regimes in the coexistence region, that the linear stability analysis is unable to provide.

#### 4.1.4. Characterisation of the clustered dynamics

In this Paragraph we would like to examine the clustered dynamics of the neurons in more details. In particular, we wish to characterise the erratic behaviours that lead the neurons to deviate from a perfectly locked evolution, where the neurons fire every second burst.

We will first examine the evolution in time of the fraction of surviving neurons  $S(t)$  (or survival probability). As shown in figure 9,  $S(t)$  has an initial decay on the interval  $[0 : 30]$  s very well described by the following function

$$g_1(t) = \alpha_1 e^{-\sqrt{t}}, \quad (37)$$

with  $\alpha_1 = 1.65(1)$ . The initial decay of  $S(t)$  is followed at later times by an exponential tail of the form

$$g_2(t) = \alpha_2 e^{-\beta_2 t} \quad (38)$$

with  $\alpha_2 = 0.142(2)$  and  $\beta_2 = 0.1026(3)$  Hz. The functions  $g_1$  and  $g_2$  are part of the same class of survival probabilities associated to the so-called Weibull PDF [44]

$$f_p(t) = p\mu^p t^{p-1} e^{-(\mu t)^p} \quad \text{with } p \in [0, +\infty) \quad \mu > 0; \quad (39)$$

where  $g_1$  ( $g_2$ ) corresponds to  $p = 1/2$  ( $p = 1$ ). For  $p < 1$  the failure rate, the rate to emit a spike in an irregular manner, decreases over time, since the neurons that displays an irregular spiking are eliminated from the population of the regular spiking ones. The neurons remaining after this initial phase have a failure rate  $\beta_2$  that is constant over time, since their survival probability has an exponential profile, which typically emerges due to some underlying random Poissonian process.

As we will see in the following for a homogeneous network  $S(t)$  is very well described by equation (38) over the whole time interval. Thus suggesting that this decay is likely due to the action of the noise injected in the system, since this is the only source of irregularity in the homogeneous case. While the initial decay described by the function  $g_1(t)$  should be related to the heterogeneous distribution of the synaptic couplings. In summary, initially the neurons displaying failures in their periodic activity are the ones with  $J_i$  sufficiently

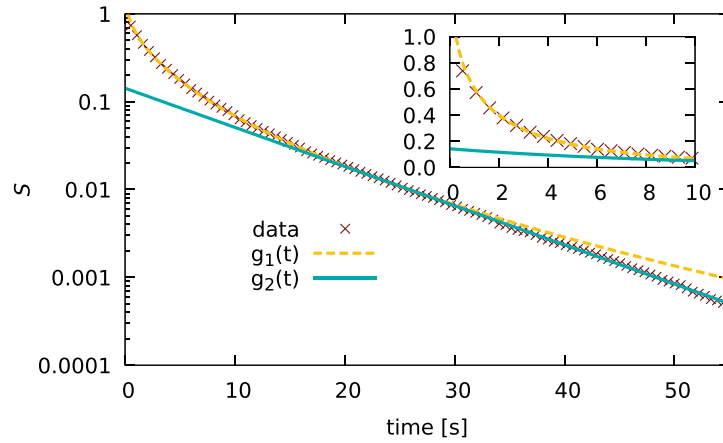


**Figure 9.** Fraction of surviving neurons  $S(t)$  versus time in a semi-logarithmic scale. We fitted the data to the function  $g_1(t)$  (37) in the time interval  $[0 : 30]$  s and to the function  $g_2(t)$  (38) in the interval  $[20 : 55]$  s. The inset shows the evolution over the first 10 seconds in a linear scale. In this case we have identified  $N_{\text{none}} = 467$  silent neurons. The data refer to a system size  $N = 200\,000$  and  $\sigma = 0.008\,42$  for the clustered regime. Other parameters as in figures 1(b) and (c).

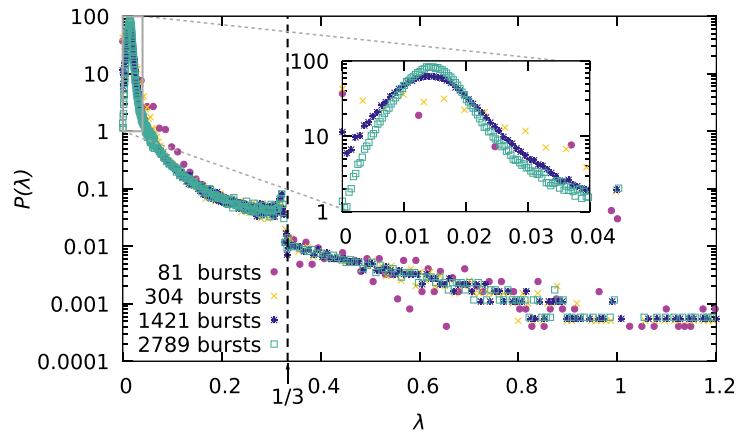


**Figure 10.** Probability distribution function  $P(\lambda)$  of the fraction of irregular spikes  $\lambda$  for different time durations in semi-logarithmic scale. The inset shows a zoom around the main peak. In this case we have removed from the estimation of the PDF  $N_{\text{none}} = 467$  silent neurons. The data refer to a system size  $N = 200\,000$  and  $\sigma = 0.008\,42$  for the clustered regime. Other parameters as in figure 1(b) and (c).

different from  $J_0$ , while the successive decay involves neurons with coupling in proximity of  $J_i = J_0$ . This aspect will be further analysed in the following, where we will correlate in more details the irregular evolution of the  $i$ th neuron to its synaptic coupling  $J_i$ .

Next, we examine the PDF  $P(\lambda)$  of the fraction  $\lambda$  of irregular spikes (28) emitted by each neuron. We report  $P(\lambda)$  in figure 10 for increasing duration of the simulations and therefore for an increasing number of population bursts.

From the figure it is evident that the PDF is converging to a limiting profile for longer duration of the measurements. This asymptotic shape reveals a peak around  $\lambda \simeq 0.0145$  corresponding to the neurons with couplings in proximity of  $J_i = J_0 = -20$ , i.e. to the maximum of the LD of the synaptic couplings. Furthermore,  $P(\lambda)$  reveals a clear discontinuity at  $\lambda = 1/3$ , whose origin will become clear in the following.

Let us now characterise in details how the fraction of irregularly emitted spikes of neuron  $i$  depends on its synaptic coupling  $J_i$ . To this aim we have estimated  $\lambda_i$ ,  $\lambda_i^E$  and  $\lambda_i^I$  for each neuron as well as the fraction  $\nu_i$  of emitted spikes with respect to the total number of population bursts ( $\nu_i$  in absence of irregularity should be  $\frac{1}{2}$ ). These quantities are shown versus the corresponding  $J_i$  as scatter plots in figure 11. It is important to notice that the scatter plots actually look like smooth functions for all the considered indicators, not much ‘scatter’ visible. This suggests the existence of a functional relationship between the measure values and the value  $J$  of the synaptic coupling.

For sufficiently small  $J_i \leq -22.73$  the neurons appear to be silent on the considered integration time scale. As shown in panels (a and d),  $\nu_i$  is growing with the synaptic coupling, apart in the locking regions. On the contrary,  $\lambda_i^I$  and  $\lambda_i$  have a non monotonic dependence on  $J_i$ , with a maximum at  $J_i = -21.44$  where



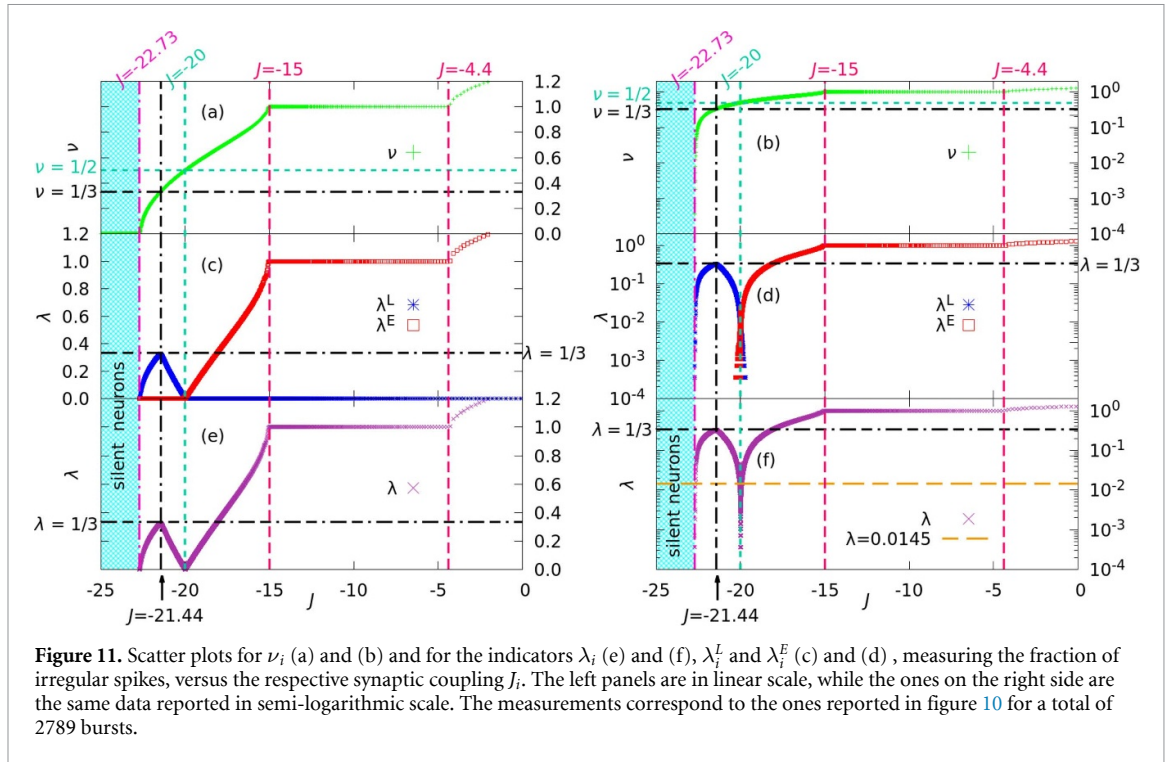


**Figure 11.** Scatter plots for  $\nu_i$  (a) and (b) and for the indicators  $\lambda_i$  (e) and (f),  $\lambda_i^L$  and  $\lambda_i^E$  (c) and (d), measuring the fraction of irregular spikes, versus the respective synaptic coupling  $J_i$ . The left panels are in linear scale, while the ones on the right side are the same data reported in semi-logarithmic scale. The measurements correspond to the ones reported in figure 10 for a total of 2789 bursts.

these parameters reach the value of exactly  $\frac{1}{3}$ .  $\lambda_i$  displays a minimum at  $J_i = J_0 = -20$ , where it attains extremely small values (see panels (c) and (d) and (e) and (f)). For larger  $J_i$  essentially  $\lambda_i \equiv \lambda_i^E$  and they are both increasing with  $J_i$ , again apart the locking intervals. As a general remark the irregularity in the periodic firing of the neurons is due to early (late) delivered spike for  $J_i < J_0$  ( $J_i > J_0$ ).

Let us now try to understand the non monotonic behaviour of  $\lambda$ . The local maximum  $\lambda_i^L = \lambda_i = \frac{1}{3}$  at  $J_i \leq -22.73$  corresponds to  $\nu_i = \frac{1}{3}$ , which means that the corresponding neurons fire very regularly at every 3rd burst. The origin of the maximum is due to the fact that for smaller  $J_i$  the neurons are firing less and less, thus the value of  $\lambda_i^L$  and  $\lambda_i$  should necessarily decrease, however for larger  $J_i$  the two parameters are also decreasing. This is due to the fact that the regular behaviour occurs whenever the neurons fire exactly every two spikes, and this state is approached by increasing  $J_i$  towards  $J_0$ .

Indeed, for  $J_i = J_0$  the rate is exactly  $\nu_i = \frac{1}{2}$  and at the same time  $\lambda_i$ ,  $\lambda_i^L$  and  $\lambda_i^E$  become quite small and close to zero (see the semi-logarithmic plots in panel (d)). In particular, from panel (f) it is evident that the neurons contributing to the peak of  $P(\lambda)$  reported in figure 10 are those with  $J_i = J_0$ , see the dashed orange line indicating the value  $\lambda = 0.0145$ , where  $P(\lambda)$  attains its maximum.

It is interesting to notice that in the interval  $J \in [-15, -4.4]$  we have a perfect locking of the activity of these neurons with the population bursting since  $\nu = 1$ , and unsurprisingly, also  $\lambda^E = 1$ . The locking region resembles an Arnold tongue 1:1, for  $J > -4.4$  the locking is lost and  $\nu$  and  $\lambda$  continues to increase. We have indications that another locking region with  $\nu = 2$  emerges at quite large  $J$ , around  $25 \leq J \leq 29$ , however our system size is too small to have a good statistics there.

Let us now come to the explanation of the discontinuity observed in figure 10 for the PDF  $P(\lambda)$  at  $\lambda \approx \frac{1}{3}$ . This is due to the fact that the maximal value of  $\lambda_L$  is  $\frac{1}{3}$ , thus for  $\lambda < \frac{1}{3}$  to the  $P(\lambda)$  contribute both early and late delivered spikes, while for  $\lambda > \frac{1}{3}$  the contribution to the irregularity is due only to early delivered spikes.

To get further insight on the microscopic dynamics induced by the synaptic couplings, we define a global phase  $\Phi$  similar to equation (19). However, instead of the spike times of the individual neurons we consider here the population burst times  $b_k$ :

$$\Phi(t) = 2\pi \frac{t - b_k}{b_{k+1} - b_k} + 2\pi k \quad \text{with } b_k \leq t b_{k+1}. \quad (40)$$

Moreover,  $\Phi(t)$  can be employed to characterise the activity of the  $i$ th neuron with respect to the network activity by defining the global phase difference associated to two successive spikes of neuron  $i$ :

$$\Delta\Phi_i(n) = \Phi(t_i^{(n+1)}) - \Phi(t_i^{(n)}). \quad (41)$$

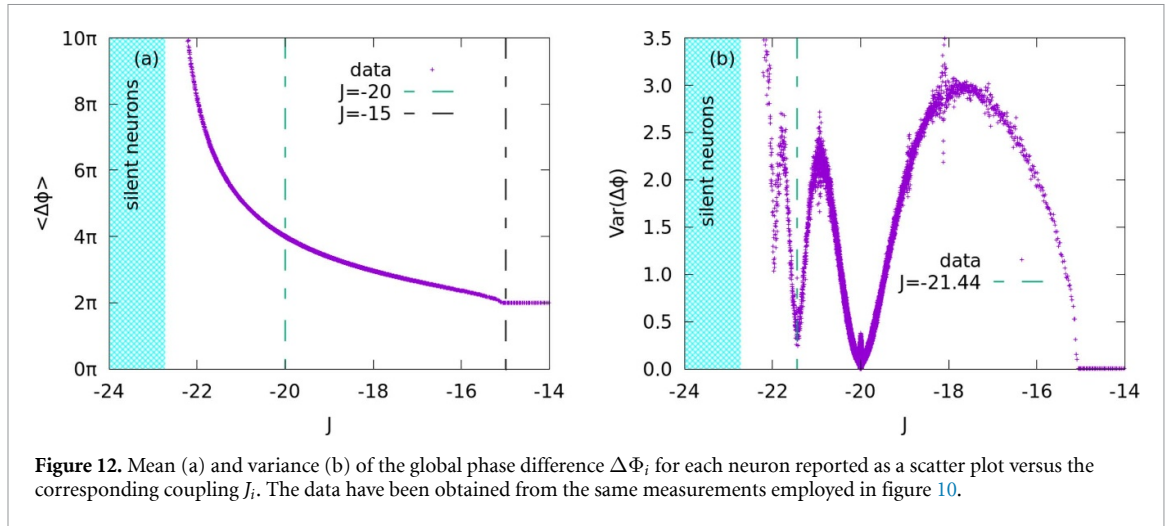


**Figure 12.** Mean (a) and variance (b) of the global phase difference  $\Delta\Phi_i$  for each neuron reported as a scatter plot versus the corresponding coupling  $J_i$ . The data have been obtained from the same measurements employed in figure 10.

In figure 12 we report the average and variance of  $\Delta\Phi_i$  estimated over all the spike times of neuron  $i$  versus the corresponding synaptic coupling  $J_i$ . A clear functional relationship emerges also in this case. As expected, the value of the mean of  $\Delta\Phi_i$  is  $4\pi$  for  $J_i = -20$  indicating that the neurons fire every second burst. For  $J_i < J_0$  ( $J_i > J_0$ )  $\Delta\Phi_i$  grows (decreases) indicating that the neurons fire slower (faster). Moreover, the phase locking at  $\Delta\Phi_i = 2\pi$  for neurons with  $J_i \in [-15, -4.4]$  is also evident from panel (a).

The analysis of the variance of  $\Delta\Phi_i$  reveals more interesting aspects. A variance close to zero suggests that the corresponding neuron fires very regularly, i.e. basically with a constant firing rate. In contrast a high variance indicates a distribution of the global phase differences  $\Delta\Phi_i$  exhibiting more peaks. As shown in figure 12(b), the variance attains its minimal value for  $J_i = -J_0$  for the regular firing neurons, for which  $\langle \Delta\Phi_i \rangle \simeq 4\pi$ . Moreover, minima in the variance are observable also whenever  $\langle \Delta\Phi_i \rangle \simeq 6\pi$  at  $J \approx -21.44$ , and also at lower  $J_i$  where  $\langle \Delta\Phi_i \rangle \simeq 8\pi$ . Furthermore, the variance vanishes in the locking region ( $J \in [-15, -4.4]$ ) where  $\langle \Delta\Phi_i \rangle = 2\pi$ . The maxima in the variance are instead observable when  $\langle \Delta\Phi_i \rangle \simeq (2k + 1)\pi$  for  $k = 0, 1, 2$ . For the case  $\langle \Delta\Phi_i \rangle \simeq 3\pi$ , we observe that the corresponding neurons emit two spikes almost in correspondence with two successive population bursts and then skip one burst. This amounts to a sequence of phase differences  $\Delta\Phi_i = 2\pi, 4\pi, 2\pi, 4\pi, \dots$ , that gives an average global phase of  $3\pi$  and a distributions of the phases with two equally relevant peaks and thus to a high variance.

We can safely affirm that the neurons tend to fire in correspondence of the bursting activity of the network, in general every two bursts, but as shown above they can present more complex combinations of locking  $n : m$  with the population bursting.

#### 4.2. Emergence of $\gamma$ -oscillations in the clustered state

The clustered state is characterised by population bursts, corresponding to COs. It is of extreme interest to understand in which frequency range these oscillations occur. In order to estimate the oscillation frequency we evaluate the power spectrum density (PSD) associated to the time evolution of the mean membrane potential  $v$  for heterogeneous ( $\Delta_J = 0.02$ ) and homogeneous ( $\Delta_J = 0$ ) case subject to noise of the same amplitude, namely  $\sigma = 0.00842$  (the results are reported in figure 13(a)).

For the heterogeneous case, we observe that the two neural mass models and the network simulations agree quite well among them as evident in figure 13(a). The only noticeable difference are the positions of the main peak of the PSD, that are slightly different. The main peak of the 3rd order neural mass model and of the network simulations are located both around  $f_0 \approx 50.79$  Hz, while the 2nd order neural mass reveals a peak located at  $f_0 \approx 50.95$  Hz, as visible in the inset of figure 13(a). This seems to be a general trend, since it is confirmed also for different parameter values (namely,  $J_0 = -18$  and  $\sigma = 0.01$ ) as shown in figure 13(b).

The simulations of the network with homogeneous couplings result in a PSD with a peak at a higher frequency  $f_0 \approx 52.8$  Hz, still in the vicinity of the heterogeneous peaks.

The PSD around the peak is a bit broader for the network simulations compared to the neural mass results, since the network presents also finite-size fluctuations. In the network simulations, homogeneous and heterogeneous, we observe also peaks at combinations of the first two harmonics, not present in the neural mass models, suggesting that finite-size effects can lead to combinations of these harmonics similar to the beating phenomenon.

By analysing the microscopic dynamics of the network for the same parameters in the homogeneous case, we observe that the histogram  $n_\nu$  of the single neuron firing rate  $\nu_i$  is extremely localised with a peak around

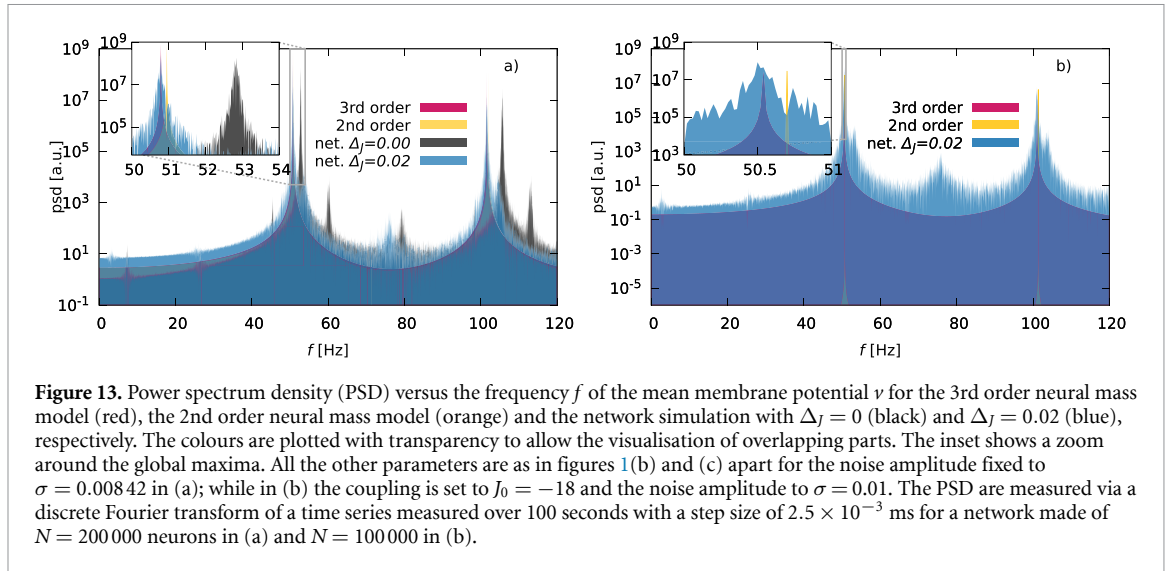


**Figure 13.** Power spectrum density (PSD) versus the frequency  $f$  of the mean membrane potential  $v$  for the 3rd order neural mass model (red), the 2nd order neural mass model (orange) and the network simulation with  $\Delta J = 0$  (black) and  $\Delta J = 0.02$  (blue), respectively. The colours are plotted with transparency to allow the visualisation of overlapping parts. The inset shows a zoom around the global maxima. All the other parameters are as in figures 1(b) and (c) apart for the noise amplitude fixed to  $\sigma = 0.00842$  in (a); while in (b) the coupling is set to  $J_0 = -18$  and the noise amplitude to  $\sigma = 0.01$ . The PSD are measured via a discrete Fourier transform of a time series measured over 100 seconds with a step size of  $2.5 \times 10^{-3}$  ms for a network made of  $N = 200\,000$  neurons in (a) and  $N = 100\,000$  in (b).

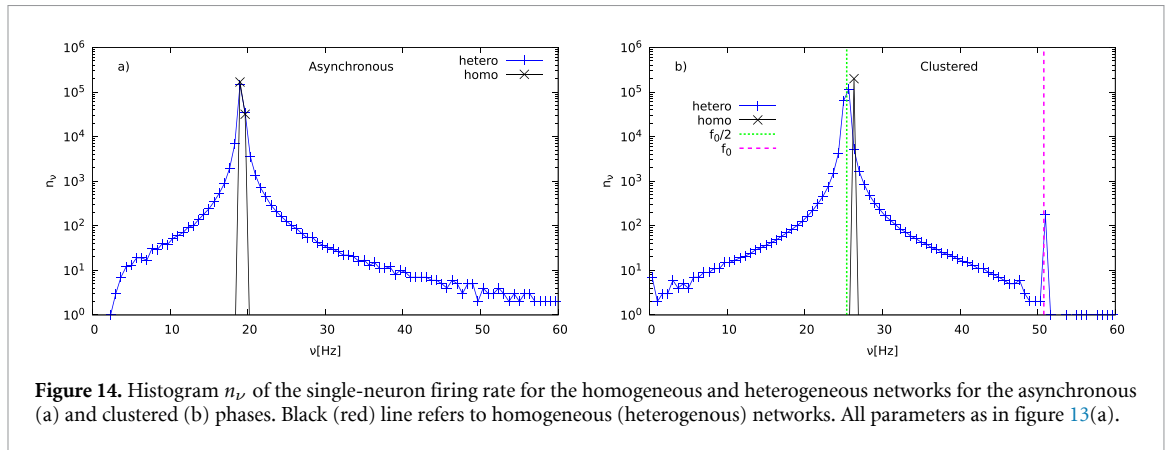


**Figure 14.** Histogram  $n_\nu$  of the single-neuron firing rate for the homogeneous and heterogeneous networks for the asynchronous (a) and clustered (b) phases. Black (red) line refers to homogeneous (heterogeneous) networks. All parameters as in figure 13(a).

$\nu_0 \approx 19.27$  Hz ( $\nu_0 \approx 26.41$  Hz) for the asynchronous (clustered) state (see figure 14(a)). These data confirm that in the clustered regime the neurons mostly fire every two population bursts, since the frequency of COs is  $f_0 \approx 52.8$  Hz. In the heterogeneous case, the situation is more complex, as shown in figure 14(b) the histogram of the firing rates has a main peak at  $f_0/2$  with symmetric tails at lower and higher frequencies and a secondary peak at  $f_0$ , where  $f_0 \approx 50.79$  Hz. These data confirm the previously reported analysis for the heterogeneous model performed in section 4.1.4. The heterogeneity in the couplings is essentially responsible for the distributed firing rates. Furthermore, the most part of the neurons fire every second bursts, but a small group is locked to the population activity.

Increasing the noise amplitude only changes the frequency slightly, e.g. a noise of  $\sigma = 0.03$  results in a frequency around 52.44 Hz for the 3rd order mean-field neural mass, this means that we observe  $\gamma$ -oscillations in the whole region of coexistence.

## 5. Summary and outlook

We have shown that for a globally coupled inhibitory network of QIF neurons the presence of independent Gaussian noise promotes the emergence of COs both for heterogeneous and homogeneous synaptic couplings. For sufficiently large synaptic coupling  $|J_0|$ , the observed oscillations emerge at some critical noise amplitude  $\sigma_c$  via a sub-critical Hopf bifurcations giving rise to a region of coexistence among stationary and oscillatory dynamics. For the homogeneous (heterogeneous) case the coexistence is observable from zero (a finite) noise amplitude up to  $\sigma_c$ .

In the heterogeneous case the analysis is based on the comparison of the results obtained via a direct integration of large spiking QIF networks and of the corresponding neural mass models. In the examined noise range we observe a quite good agreement among network simulations and mean-field results obtained via the pseudo-cumulant expansion arrested to the third order [21]. The second-order neural mass model fails to reproduce the simulations for sufficiently large noise amplitudes.

The neural mass model (at the third order) captures well the macroscopic behaviour of the network induced by noise and heterogeneity, however being a mean-field model cannot reproduce the microscopic dynamics, for this we should rely on numerical simulations.

The observed collective oscillations are population bursts, where roughly half of the neurons fire in alternation in correspondence of each single collective event. However, there are irregularities to this behaviour. In the heterogeneous case we observe that initially the rate at which the surviving neurons emit a spike in an irregular manner decreases over time and successively it becomes constant, i.e. it becomes a Poissonian process in the long run. The origin of the initial behaviour is due to the heterogeneity in the synaptic couplings, while the following phase is due to the presence of the Gaussian noise. Indeed in the homogenous case we observe only the second phase.

Furthermore, for heterogenous couplings we observe that the regular behaviour of the neurons, i.e. firing every two population bursts, is observable only for synaptic couplings corresponding to the median of the distribution. For sufficiently large inhibitory couplings we have silent neurons, while neurons displaying a 1:1 locking with the population bursts are observable in a wide interval of synaptic couplings.

In order to characterise the stability of the asynchronous regime we have introduced a new criterion based on the long-term evolution of the system, once the stationary configuration corresponding to the asynchronous regime has been subject to a non-infinitesimal global deformation. This criterion allows to identify the basins of attraction of the two coexisting regimes, therefore resembling the basin stability analysis [24]. Furthermore, the method captures with very good accuracy the Hopf and saddle-node bifurcation points delimiting the coexistence regime in the heterogenous and homogenous cases. This criterion can represent a useful alternative to the linear stability analysis and find application in the context of complex networks for the characterisation of their dynamical regimes.

The nature of the noise is fundamental in order to observe the reported phenomena. Indeed, in appendix A we have shown that for Lorentzian distributed white noise the corresponding low-dimensional neural mass model [45, 46] exhibits only a stable foci and no oscillatory regime, as we have also verified via network simulations.

Clustering phenomena similar to the one here analysed have been reported in [5] for globally coupled inhibitory homogenous networks for conductance based and current based neural models in presence of Gaussian noise. However, at variance with our model the authors considered post-synaptic potentials of finite duration and not instantaneous synapses, as in the present case. The emergence of COs in absence of a delay or of a finite synaptic time scale is peculiar of inhibitory QIF networks, as previously shown in [47].

As we have shown for the chosen parameters the frequency of the COs is in the  $\gamma$ -band, therefore the present model can be employed to analyse the emergence of transitory  $\gamma$ -bursts coexisting with asynchronous dynamics observed in many experiments [14–17]. In particular, our model can represent a more realistic alternative to the damped harmonic oscillator driven by noise employed in [16] to reproduce the emergence of spontaneous  $\gamma$ -cycles in awake primate visual cortex (V1). Finally, the indicators we have introduced in Paragraph 2.3.3 to characterise the regularity/irregularity of the single-neuron dynamics with respect to the global activity can find applications in the analysis of spiking events with respect to the Local Field Potential evolution in experimental data.

## Data availability statement

All data that support the findings of this study are included within the article (and any supplementary files).

## Acknowledgments

We thank D S Goldobin for extremely useful interactions and N La Miciotta, S Olmi, A Pikovsky for valuable discussions as well as Yvonne Feld for helping us in realising several figures. The simulations were performed at the HPC Cluster CARL, located at the University of Oldenburg (Germany) and funded by the DFG through its Major Research Instrumentation Program (INST 184/157-1 FUGG) and the Ministry of Science and Culture (MWK) of the Lower Saxony State. This work also used the Scientific Compute Cluster at GWDG, the joint data center of Max Planck Society for the Advancement of Science (MPG) and University of Göttingen. Y F received financial and logistical support by the German Academic Scholarship Foundation (Studienstiftung des Deutschen Volkes). A T received financial support by the Labex MME-DII (Grant No. ANR-11-LBX-0023-01), by the ANR Project ERMUNDY (together with Y F) (Grant No. ANR-18-CE37-0014), and by CY Generations (Grant No ANR-21-EXES-0008), all part of the French program Investissements d'avenir. Y F thanks the Istituto dei Sistemi Complessi (CNR) in Sesto Fiorentino, Italy and the Laboratoire de Physique Théorique et Modélisation, CY Cergy Paris Université, in

Cergy-Pontoise, France for the hospitality offered during 2022 and 2023, where part of this work has been developed.

## Appendix A. Lorentzian noise

It is worth mentioning that, by assuming that the white noise terms  $\xi_i(t)$  in (1) are Lorentzian distributed, it is still possible to obtain the corresponding low-dimensional neural mass model in an exact manner [45, 46]. In particular, by assuming that the  $\xi_i(t)$  random terms follow a LD centred in zero and with HWHM  $\Gamma$ , one can obtain the following two-dimensional neural mass model [46]

$$\dot{r} = 2rv + (\Delta_\eta + \Gamma + \Delta_J r) \pi^{-1} \quad \text{and} \quad \dot{v} = \eta_0 + J_0 r - \pi^2 r^2 + v^2, \quad (\text{A.1})$$

which is identical to equation (31) apart for the  $\Gamma$  term that contributes exactly as the HWHM  $\Delta_\eta$  of the neural excitabilities  $\{\eta_i\}$  to the mean-field dynamics. Therefore, in the thermodynamic limit the Lorentzian noise can be assimilated to a quenched disorder in the heterogeneities as shown also in [45, 46]. This implies that the neural mass model equation (A.1) displays only stable foci solutions as in the deterministic situation equation (31) and no collective oscillations are observable, contrary to the case where the noise is Gaussian distributed.

## Appendix B. Homogeneous synaptic couplings

As we have seen in section 3 for the case with homogeneous couplings, i.e.  $\Delta_J = \Delta_\eta = 0$ , the linear stability of the mean-field model predicts that the asynchronous state is unstable whenever the noise amplitude is finite. However, the mean-field approach is no more strictly valid in the fully homogenous case, since the Ott–Antonsen manifold [26] is no more attractive in such a case [48]. Therefore, we will limit to network simulations in order to numerically investigate the stability of the asynchronous state as well as possible coexistence regime with a collective oscillatory dynamics.

### B.1. The clustering transition

To this aim we performed quasi-adiabatic simulations of the QIF network by varying the noise amplitude  $\sigma$  and by evaluating the variance  $\Sigma_v$  of the mean membrane potential  $v$ , analogously to the analysis done in the heterogeneous case, whose results have been reported in figure 2. In the present case, by increasing adiabatically  $\sigma$  in the interval  $[0, 0.015]$  we observe that the asynchronous regime appears to remain stable up to noise amplitude  $\sigma_c \simeq 0.011$ , while for larger noise COs emerge. Successively, by decreasing  $\sigma$  the oscillatory regime remains stable down to  $\sigma = 0$ , thus we have a coexistence regime in the whole interval  $\sigma \in [0, 0.011]$ , as shown in figure B1. Note the contrast with the heterogeneous case where, in the absence of noise, only the asynchronous regime was observable.

The oscillatory regime is once more a clustered regime, where the neurons fire in population bursts and each burst involves almost half of the population.

### B.2. Stability of the asynchronous regime

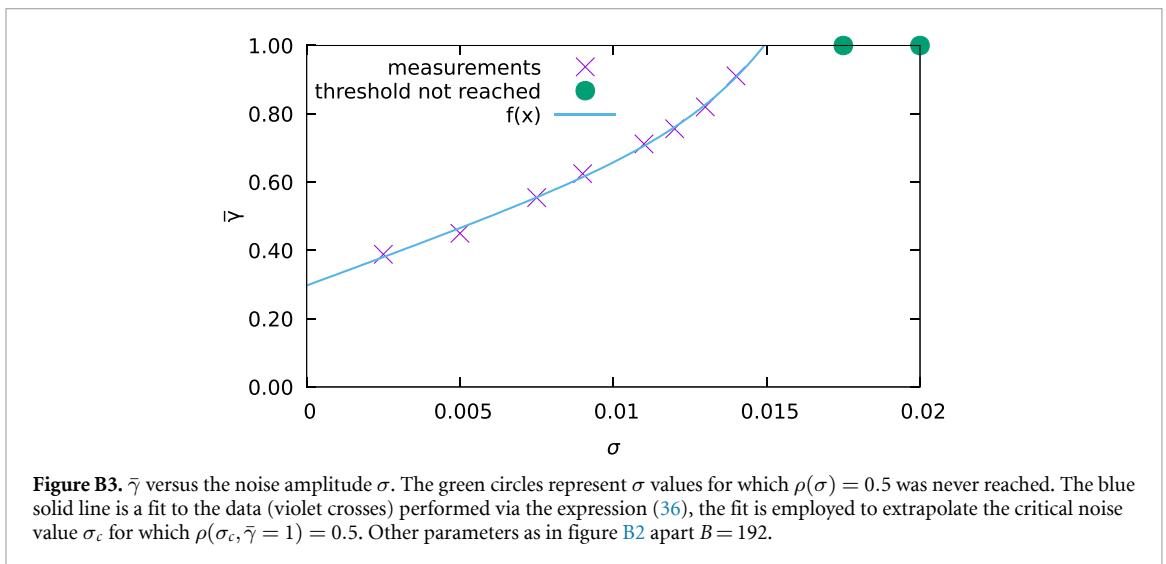
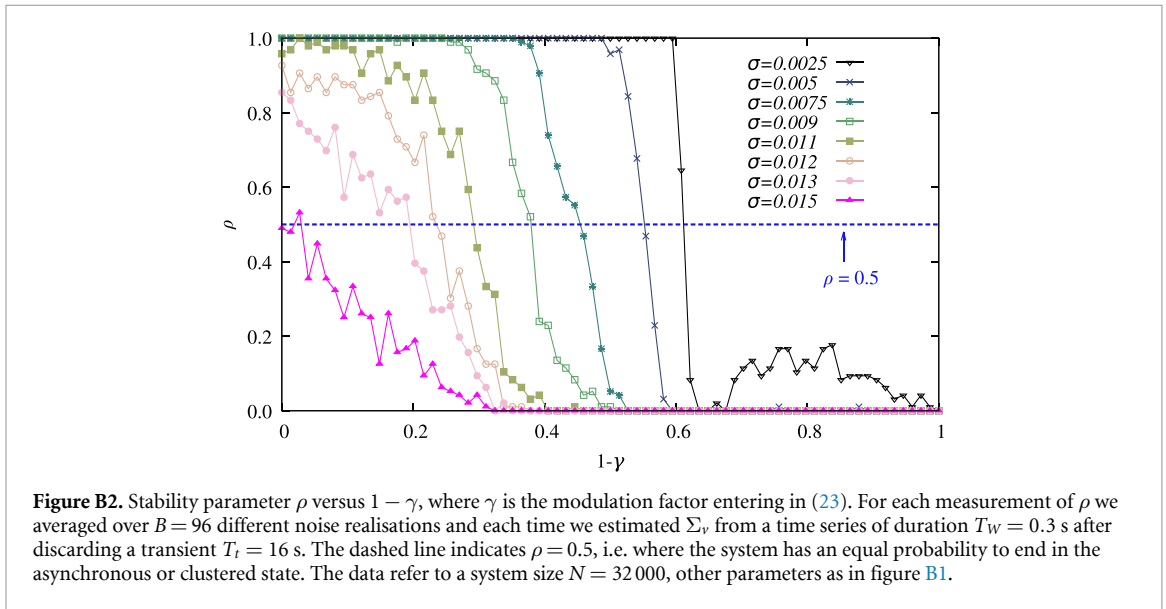
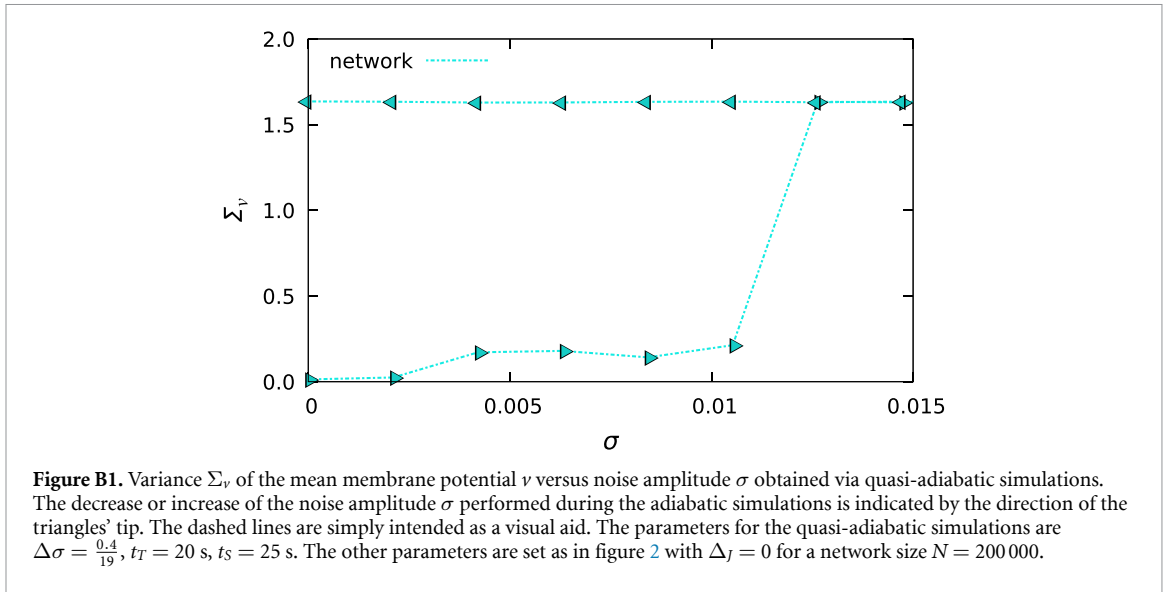
Let us now analyse, how the stability of the asynchronous state depends on the noise amplitude. To perform this analysis we have employed (as in section 4.1.3) the indicator  $\rho = \rho(\gamma)$  introduced in equation (24) as a function of the parameter  $\gamma$ . The corresponding results are reported in figure B2 for various noise amplitudes  $\sigma \in [0, 0.015]$ .

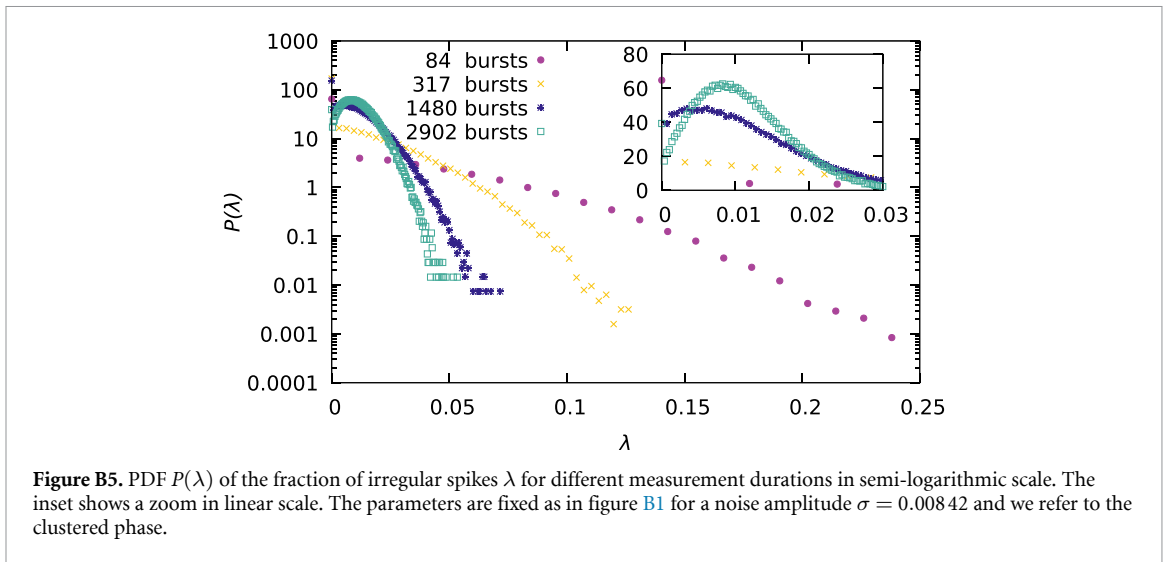
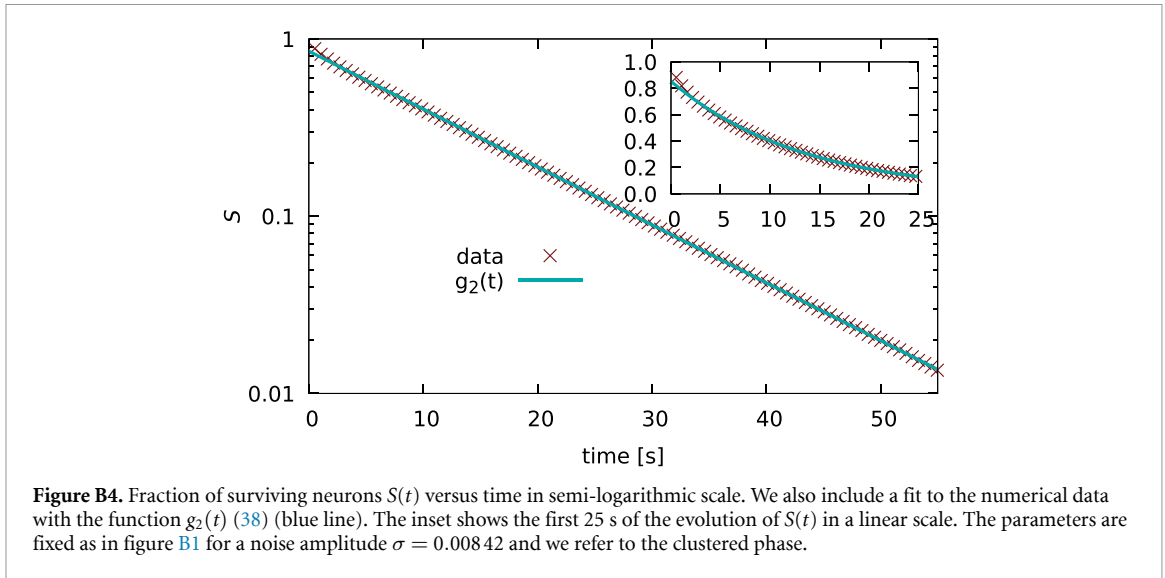
The main difference with respect to the heterogenous case, is that now even for the smallest noise amplitude considered, namely  $\sigma = 0.0025$ , for a sufficiently large distortion of the LD (namely,  $\gamma > 0.4$ ) will destabilise the asynchronous state. This is a further confirmation that the clustered state is always stable, as already shown in figure B1. For increasing noise amplitudes the asynchronous state gets destabilised for larger and larger  $\gamma$  values and for  $\sigma > 0.011$  even for  $\gamma = 1$ . Thus indicating that this is the critical noise amplitude above which only the clustered regime can be observed on the long-time limit.

In analogy to what done in section 4.1.3, to better characterise this transition, we will estimate for various noise amplitudes the value  $\bar{\gamma}$  for which  $\rho(\bar{\gamma})$  crosses  $\frac{1}{2}$ . In particular, we measured  $\bar{\gamma}$  by using  $B = 192$  to obtain a better accuracy. The results are displayed in figure B3, by performing a fit of the data to the function (36) we obtained the following parameter value  $a = -0.21(6)$ ,  $b = 376(205)$ ,  $c = 33(6)$  and  $\sigma_c = 0.0149(3)$ . Thus obtaining a critical noise amplitude consistent with the previous estimations.

### B.3. Characterisation of the clustered dynamics

Analogously to the heterogenous case the oscillatory dynamics is characterised by neurons firing alternately in the two population bursts. To measure the irregularity in this dynamics, we have examined, as in the





heterogeneous case, the fraction of surviving neurons  $S(t)$  defined as in equation (29), for the same noise amplitude  $\sigma = 0.00842$ . We now observe that  $S(t)$  can be well reproduced by a simple exponential decay equation (38) with parameters  $\alpha_2 = 0.853(2)$  and  $\beta_2 = 0.0752(6)$  Hz, see figure B4. The mean lifetime of the periodic regular regime is now of the order of 13.3 s, definitely longer than in the heterogeneous case. Since the only source of irregularity is now the noise, we confirm that the emergence of the irregularities in the firing process follows a Poissonian process. Furthermore, in contrast with the heterogeneous case we did not observe any silent neurons, since none of the neurons receive very large inhibitory post-synaptic potentials, because the amplitude of the synaptic weight is the same for all neurons.

Next, we have estimated  $P(\lambda)$ , i.e. the PDF of the fraction  $\lambda$  of irregular spikes obtained for each neuron, this is reported in figure B5. We have integrated the network for the same time duration as in figure 10, however due to the slightly higher frequency of the COs measured in the homogeneous case we observe more bursts.

In this case the PDF for  $\lambda^E$  and  $\lambda^L$  are identical (not shown) and this is clearly due to the absence of heterogeneity in the network. The noise induces with equal probability irregularities due to early or late spiking.

For increasing duration of the measurements we observe that  $P(\lambda)$  tends to get more and more localised around the maximum located at  $\lambda = \lambda_0 \approx 0.01$ . Due to the central limit theorem we expect that the function  $P(\lambda)$  has a Gaussian profile (limited to  $\lambda > 0$ ) with a standard deviation  $\sigma$  scaling as  $1/\sqrt{T}$ , where  $T$  is the time duration. Indeed, by considering only values of  $\lambda > \lambda_0$  we have verified that  $\ln P(\lambda) = A + \frac{(\lambda - \lambda_0)^2}{2\sigma^2}$  with  $\sigma \propto T^\xi$  where  $\xi = -0.52 \pm 0.02$  for the data reported in figure B5.

## Appendix C. Details on the numerical simulations

For the heterogenous case, in order to compare the results of the network simulations with the neural mass models [21] we consider synaptic couplings following a LD  $h(J_i)$  with median  $J_0$  and half width at half maximum (HWHM)  $\Delta_J$ , that we fix deterministically as follows

$$J_i = \tan\left(\frac{\pi(2i - N - 1)}{2(N + 1)}\right) \Delta_J + J_0 \quad \forall i \in \{1, 2, \dots, N\}, \quad (\text{C.1})$$

to avoid spurious effects related to extreme values of the couplings and to allow for a faster convergence at sufficiently large system sizes towards the corresponding mean-field results as previously shown e.g. in [20, 49]. It should be noticed that even for a LD centred at a quite negative value, namely  $J_0 = -20$  as in our case, a small number of positive coupling is expected. For the parameter values used in this paper ( $\Delta_J = 0.02$ ) the percentage of excitatory synaptic coupling is 0.032%, therefore we can consider their influence on the macroscopic dynamics as negligible.

The initial values of the membrane potentials are deterministically chosen as in equation (23) from the LD expected in the thermodynamic limit (6) for the asynchronous state. Note that, to avoid correlations between  $V_i$  and  $J_i$  that would result from the previous deterministic equations, the list of  $J_i$  values is shuffled before creating the initial state of the network.

In order to analyse the transition from the asynchronous to the partially synchronised regime due to the noise, we perform simulations where the noise amplitude is varied quasi-adiabatically. In particular, we start from some initial noise value, typically  $\sigma = 0$ , and we simulate the models for a certain time interval  $t_S$ , after discarding a transient time  $t_T$ . The quantities of interest are evaluated only during the interval  $t_S$ . Then we increase the noise amplitude by an amount  $\Delta\sigma$  and we repeat the previous procedure by an initial condition that is the last configuration obtained at the previous step. The noise is increased in steps of amplitude  $\Delta\sigma$  up to some maximal value is reached. Then the procedure is repeated by decreasing the noise at each simulation step by  $\Delta\sigma$  until the initial noise value is recovered.

As already mentioned, for the QIF model the threshold value would be  $V_{\text{th}} = +\infty$  and the reset one  $V_{\text{re}} = -\infty$ , it is possible to take in account exactly the integration among these extrema in absence of noise if the neurons are supra-threshold by employing event driven techniques [50, 51]. However, in presence of noise we should perform usual clock driven simulations by employing finite threshold and reset values as suggested in [20].

In particular, we implement the finite threshold crossing and the spike emission as follows. Whenever  $V_i(t) > V_{\text{th}}$ , the neuron enter in a refractory period of duration  $T_R = 2/V_i$ , after this phase the membrane potential is resetted to  $V_i(t + T_R) = -V_i(t)$ . Thus employing a variable resetting value related to the neuron evolution, this avoids spurious synchronisation phenomena induced by using the same reset value for all neurons as suggested in [20]. Furthermore, the neuron  $i$  will fire at a time  $t + T_R/2$  that approximately corresponds to the time it would reach  $+\infty$  as shown in [20]. Somehow, the usage of finite thresholds and reset value is less mathematically accurate, but it reflects more the dynamics of real neurons [52].

To simulate the network model we have numerically integrated the stochastic differential equation (1) by employing a clock driven scheme. In particular we have employed the Heun method [53] for its higher accuracy in the treatment of the deterministic part with respect to a standard Euler scheme.

The iterative Heun method [53] applied to our network model reads as :

$$k_i = J_i s + \Delta_t \left( (v_i(t))^2 + \eta_i \right) \quad (\text{C.2})$$

$$l_i = \sqrt{2\Delta_t\sigma^2}\Xi_i \quad (\text{C.3})$$

$$v_i(t + \Delta_t/2) = v_i(t) + l_i + k_i \quad (\text{C.4})$$

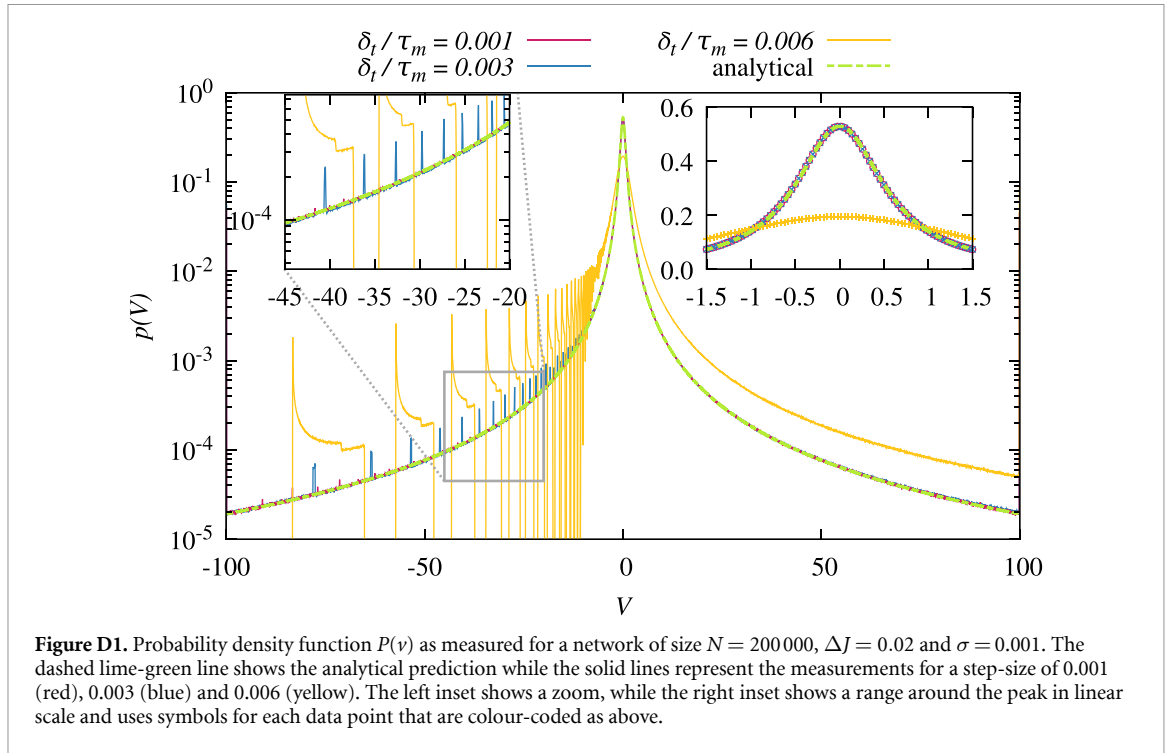
$$v_i(t + \Delta_t) = v_i(t) + \left( (v_i(t + \Delta_t/2))^2 + \eta_i \right) \frac{\Delta_t}{2} + \frac{J_i s + k_i}{2} + l_i, \quad (\text{C.5})$$

where  $V_i(t)$  are the membrane potentials,  $k$  and  $l$  are auxiliary variables, and  $\Xi_i$  is a Gaussian random number with zero mean and unitary standard deviation that is drawn separately for each neuron. Moreover  $\Delta_t$  is the integration time step, whose choice will be discussed in the next appendix, and  $s$  represents the network activity and it is the number of spikes emitted in the network in the interval  $\Delta_t$  divided by  $N$ .

## Appendix D. Selection of the integration time step

For the numerical integration of the network model we need to select an optimal time step  $\Delta_t$ , which should lead to high accuracy in the integration joined to a minimal computational cost.





In deterministic systems this choice is quite simple, one just select the largest time step for which the integrated orbits converge to the same value up to some accuracy. In a stochastic system this cannot happen, therefore we rely on a different concept.

In the present case, we know from the mean-field approach that in the asynchronous regime for sufficiently small noise values  $\sigma < \sigma_{\text{SN}}$  the system should always relax towards a PDF of the membrane potential that is a LD, namely

$$p(V) = \frac{1}{\pi} \frac{\Delta_V}{\Delta_V^2 + (V - V_0)^2}. \quad (\text{D.1})$$

with  $V_0 = v^*$  and  $\Delta_V = \pi r^*$ , where  $(v^*, r^*)$  are the fixed point solutions of the neural mass model equation (16). Therefore, we considered a small noise value  $\sigma = 0.001 < \sigma_{\text{SN}}$  and for different integration time steps  $\Delta_t$  we have verified if the distribution of the membrane potentials converge to (D.1) or not.

In particular, we initialised the simulation always with membrane potentials distributed as in (D.1), then we simulate the system for a time interval of 1.2 s and every 0.12 ms we accumulate the instantaneous values of the membrane potentials in a histogram of 5000 bins with  $V \in [-100, 100]$ . We do not consider the neurons in their refractory periods to prevent from unphysical overestimations of large  $V$  values. From the final histogram we obtain the PDFs shown in figure D1 for three different  $\Delta_t/\tau_m = 1 \times 10^{-3}; 3 \times 10^{-3}; 6 \times 10^{-3}$  together with the expected PDF (D.1).

As evident from figure D1, the larger time-step leads to clear artefacts in the estimation of the PDF. Already by considering  $\Delta_t/\tau_m = 3 \times 10^{-3}$  leads to a noticeable improvement, in particular the right inset of figure D1 reporting  $p(V)$  in linear scale around the maximum show essentially no differences among (D.1) and the estimated PDFs with  $\Delta_t/\tau_m \leq 3 \times 10^{-3}$ . However, in the semi-logarithmic scale (left inset and main figure) the numerically estimated PDF for  $\Delta_t/\tau_m = 3 \times 10^{-3}$  still presents numerical artefacts for sufficiently negative  $V$  values.

For a time step  $\Delta_t/\tau_m = 1 \times 10^{-3}$ , we cannot notice any artefact and essentially we have a perfect coincidence with the theoretical PDF (D.1). We can already conclude that this time step give a sufficient accuracy to the simulations, however to be on the safe side we opted for  $\Delta_t/\tau_m = 2.5 \times 10^{-4}$ .

## ORCID iDs

Yannick Feld <https://orcid.org/0000-0003-4305-0430>

Alexander K Hartmann <https://orcid.org/0000-0001-6865-5474>

Alessandro Torcini <https://orcid.org/0000-0003-4884-3253>

## References

- [1] Winfree A T 1967 *J. Theor. Biol.* **16** 15–42
- [2] Kuramoto Y 1975 Self-entrainment of a population of coupled non-linear oscillators *Int. Symp. on Mathematical Problems in Theoretical Physics* ed H Araki (Springer) pp 420–2
- [3] Manrubia S C, Mikhailov A S and Zanette D 2004 *Emergence of Dynamical Order: Synchronization Phenomena in Complex Systems* vol 2 (World Scientific)
- [4] Wang X J and Buzsáki G 1996 *J. Neurosci.* **16** 6402–13
- [5] Brunel N and Hansel D 2006 *Neural Comput.* **18** 1066–110
- [6] Mann E O and Paulsen O 2007 *Trends Neurosci.* **30** 343–9
- [7] Bartos M, Vida I and Jonas P 2007 *Nat. Rev. Neurosci.* **8** 45–56
- [8] Goldobin D S and Pikovsky A 2005 *Phys. Rev. E* **71** 045201
- [9] Nakao H, Arai K and Kawamura Y 2007 *Phys. Rev. Lett.* **98** 184101
- [10] Gil S, Kuramoto Y and Mikhailov A S 2010 *Europhys. Lett.* **88** 60005
- [11] Lai Y M and Porter M A 2013 *Phys. Rev. E* **88** 012905
- [12] Mainen Z F and Sejnowski T J 1995 *Science* **268** 1503–6
- [13] Sosnovtseva O, Fomin A, Postnov D and Anishchenko V 2001 *Phys. Rev. E* **64** 026204
- [14] Buzsáki G and Draguhn A 2004 *Science* **304** 1926–9
- [15] Susin E and Destexhe A 2021 *PLOS Comput. Biol.* **17** e1009416
- [16] Spyropoulos G et al 2022 *Nat. Commun.* **13** 2019
- [17] Douchamps V, di Volo M, Torcini A, Battaglia D and Goutagny R 2024 *Nat. Commun.* **15** 1849
- [18] Ermentrout B 2008 *Scholarpedia* **3** 1398
- [19] Ermentrout G B and Kopell N 1986 *SIAM J. Appl. Math.* **46** 233–53
- [20] Montbrió E, Pazó D and Roxin A 2015 *Phys. Rev. X* **5** 021028
- [21] Goldobin D S, di Volo M and Torcini A 2021 *Phys. Rev. Lett.* **127** 038301
- [22] Coombes S 2023 *Front. Appl. Math. Stat.* **9** 1128224
- [23] Hartmann A K 2015 *Big Practical Guide to Computer Simulations* (World Scientific)
- [24] Menck P J, Heitzig J and Kurths N M J 2013 *Nat. Phys.* **9** 89–92
- [25] Izhikevich E M 2010 *Dynamical Systems in Neuroscience (Computational Neuroscience Series)* (The MIT Press)
- [26] Ott E and Antonsen T M 2008 *Chaos* **18** 037113
- [27] Luke T B, Barreto E and So P 2013 *Neural Comput.* **25** 3207–34
- [28] Laing C R 2014 *Phys. Rev. E* **90** 010901
- [29] Butcher J C 2008 *Numerical Methods for Ordinary Differential Equations* 2nd edn (Wiley)
- [30] Kralemann B, Cimponeriu L, Rosenblum M, Pikovsky A and Mrowka R 2007 *Phys. Rev. E* **76** 055201
- [31] Dolmatova A V, Goldobin D S and Pikovsky A 2017 *Phys. Rev. E* **96** 062204
- [32] Kuramoto Y 1984 *Chemical Oscillations, Waves and Turbulence* (Springer)
- [33] Daido H 1992 *Prog. Theor. Phys.* **88** 1213–8
- [34] Strogatz S H 2000 *Physica D* **143** 1–20
- [35] Acebrón J A, Bonilla L L, Pérez Vicente C J, Ritort F and Spigler R 2005 *Rev. Mod. Phys.* **77** 137–85
- [36] Olmi S and Torcini A 2016 *Dynamics of Fully Coupled Rotators With Unimodal and Bimodal Frequency Distribution* (Springer) pp 25–45
- [37] Denis G 2023 private communication
- [38] Kim H, Lee S H and Holme P 2016 *Phys. Rev. E* **93** 062318
- [39] Mitra C, Choudhary A, Sinha S, Kurths J and Donner R V 2017 *Phys. Rev. E* **95** 032317
- [40] Feld Y and Hartmann A K 2019 *Chaos* **29** 113103
- [41] Nauck C, Lindner M, Schürholt K, Zhang H, Schultz P, Kurths J, Isenhardt I and Hellmann F 2022 *New J. Phys.* **24** 043041
- [42] Witthaut D, Hellmann F, Kurths J, Kettemann S, Meyer-Ortmanns H and Timme M 2022 *Rev. Mod. Phys.* **94** 015005
- [43] Cox D R and Oakes D 1984 *Analysis of Survival Data* vol 21 (CRC Press)
- [44] Carroll K J 2003 *Control. Clin. Trials* **24** 682–701
- [45] Cestnik R and Pikovsky A 2022 *Chaos* **32** 113126
- [46] Clusella P and Montbrió E 2024 *Phys. Rev. E* **109** 014229
- [47] Di Volo M and Torcini A 2018 *Phys. Rev. Lett.* **121** 128301
- [48] Pikovsky A and Rosenblum M 2008 *Phys. Rev. Lett.* **101** 264103
- [49] Ciszak M, Marino F, Torcini A and Olmi S 2020 *Phys. Rev. E* **102** 050201
- [50] Tonnelier A, Belmabrouk H and Martinez D 2007 *Neural Comput.* **19** 3226–38
- [51] Goldobin D S, di Volo M and Torcini A 2023 *bioRxiv* (<https://doi.org/10.1101/2023.11.12.566734>)
- [52] Koch C 2004 *Biophysics of Computation: Information Processing in Single Neurons* (Oxford University Press)
- [53] San Miguel M and Toral R 2000 *Stochastic Effects in Physical Systems* (Springer) pp 35–127